Influence of transport on two-dimensional model simulations: 1. Long lived tracers

Eric L. Fleming,[1] Charles H. Jackman, David B. Considine,[2]

and Richard S. Stolarski
NASA Goddard Space Flight Center, Greenbelt, Maryland

Received _____; accepted _____

Submitted version: October 12, 1999

Short title: TRACER SENSITIVITY TO 2-D MODEL TRANSPORT

---

[1]Also at Steven Myers and Associates Corporation, Arlington, Virginia.

[2]Also at Department of Meteorology, University of Maryland, College Park.

Abstract.

In this study, we examine the sensitivity of long lived tracers to changes in the base transport components in our 2-D model. Changes to the strength of the residual circulation in the upper troposphere and stratosphere and changes to the lower stratospheric K_{zz} had similar effects in that increasing the transport rates decreased the overall stratospheric mean age, and increased the rate of removal of material from the stratosphere. Increasing the stratospheric K_{yy} increased the mean age due to the greater recycling of air parcels through the middle atmosphere, via the residual circulation, before returning to the troposphere. However, increasing K_{yy} along with self-consistent increases in the corresponding planetary wave drive, which leads to a stronger residual circulation, more than compensates for the K_{yy}-effect, and produces significantly younger ages throughout the stratosphere. Simulations with very small tropical stratospheric K_{yy} decreased the globally averaged age of air by as much as 25% in the middle and upper stratosphere, and resulted in substantially weaker vertical age gradients above 20 km in the extratropics. We found only very small stratospheric tracer sensitivity to the magnitude of the horizontal mixing across the tropopause, and to the strength of the mesospheric gravity wave drag and diffusion used in the model. We also investigated the transport influence on chemically active tracers and found a strong age-tracer correlation, both in concentration and calculated lifetimes.

The base model transport gives the most favorable overall comparison with a variety of inert tracer observations, and provides a significant improvement over our previous 1995 model transport. Moderate changes to the base transport were found to provide modest agreement with some of the measurements. Transport scenarios with residence times ranging from moderately shorter to slightly longer relative to the base case simulated N_2O lifetimes that were within the observational estimates of *Volk et al.* [1997]. However, only scenarios with rather fast transport rates were comparable with the Volk *et al.* estimates of $CFCl_3$ lifetimes. This is inconsistent with

model-measurement comparisons of mean age in which the base model or slightly slower transport rates compared the most favorably with balloon SF_6 data. For all comparisons shown, large transport changes away from the base case resulted in simulations that were outside the range of measurements, and in many cases, far outside this range.

1. Introduction

Two-dimensional (2-D) chemistry and transport models have been used extensively to study the natural and man-induced changes in the middle atmosphere. Of fundamental importance in 2-D modeling is the proper representation of the zonally averaged transport fields. These include a mean advective component, usually represented by the residual circulation of the transformed Eulerian mean (TEM) formulation, and a diffusion tensor which parameterizes the eddy flux effects. This diffusion is designed to mimic the zonally averaged tracer mixing effects of three-dimensional (3-D) planetary wave dissipation, small scale gravity wave breaking, and convective overturning.

Over the past two decades, advances in 2-D model transport have involved the development of parameterizations of the various eddy processes. For example, the zonal mean momentum forcing and horizontal diffusion (K_{yy}) induced by planetary waves can be determined empirically, either directly from 3-D meteorological fields, or inferred from the diabatic circulation using observed temperatures and heating rates [e.g., *Newman et al.*, 1988]. These planetary wave quantities can also be computed theoretically from a wave breaking parameterization [*Garcia*, 1991]. Other parameterizations compute the wave drag and vertical diffusion (K_{zz}) of breaking gravity waves in the mesosphere [*Lindzen*, 1981], and the momentum deposition due to Kelvin wave absorption in the tropical upper stratosphere associated with the semiannual oscillation (SAO) [*Dunkerton*, 1979]. Other studies have used long lived tracer observations to estimate dynamical quantities in the tropical stratosphere [e.g., *Hall and Waugh*, 1997; *Mote et al.*, 1998]. These advances have enabled 2-D models to better simulate the overall zonal mean flow structure and general dynamical features seen in observations of long lived species such as CH_4 and N_2O [e.g., *Garcia and Solomon*, 1985; *Gray and Pyle*, 1987; *Brasseur et al.*, 1990; *Choi and Holton*, 1991; *Yang et al.*, 1991; *Garcia et al.*, 1992; *Ko et al.*, 1993; *Bacmeister et al.*, 1995; *Nightingale et al.*, 1996; *Jackman et al.*, 1996].

Since chemically active species (e.g., CH_4, N_2O) can hide some of the transport inadequacies in models [e.g., *Hall et al.,* 1999], a more thorough evaluation of model transport accuracy can be made by comparing models with observations of inert tracers. These include radioactive carbon-14 (^{14}C) which has a source region in the NH middle and high latitude lower stratosphere similar to high speed civil transport (HSCT) emissions. Another useful transport diagnostic is the mean age of air (Γ), which corresponds to the mean transit time from the troposphere to a particular location in the stratosphere [e.g., *Hall and Plumb*, 1994]. The mean age is related to the stratospheric residence time and can be derived from an inert tracer with a quasi-linear increasing tropospheric mixing ratio, such as SF_6 [e.g., *Elkins et al.,* 1996; *Harnisch et al.,* 1996]. The age of air distribution in 2-D and 3-D stratospheric models has been addressed in previous investigations [e.g., *Waugh et al.,* 1997; *Bacmeister et al.,* 1998; *Hall et al.,* 1999; *Li and Waugh*, 1999].

Recent assessment studies have illustrated the strong dependence of model simulations on the stratospheric transport rates used in models [*WMO*, 1999; *Park et al.,* 1999; *Kawa et al.,* 1999; *IPCC*, 1999]. Accurate representation of transport remains a major uncertainty in model calculations. In light of this, we recently incorporated several of the afore mentioned parameterizations into a comprehensive, empirically-based transport formulation in our GSFC 2-D model and obtained significantly better agreement with tracer observations compared to previous model versions [*Fleming et al.,* 1999]. Subsequently, it is useful to understand how different aspects of the model dynamics affect the tracer simulations.

In the present paper, we build on the work of *Bacmeister et al.* [1998] and *Li and Waugh* [1999] to further examine the sensitivity of tracer simulations to changes in 2-D model transport components. We specifically investigate the dependence on the residual circulation and vertical diffusion in the upper troposphere and stratosphere, the horizontal diffusion and momentum forcing in the stratosphere, and the gravity

wave-induced drag and vertical diffusion in the upper stratosphere and mesosphere. We will show simulations of various tracers and compare these with observations. This allows us to identify the range of model transport rates that are within reasonable agreement with the real atmosphere. Simulations of ^{14}C and age of air are especially useful in diagnosing model accuracy in transporting and accumulating HSCT exhaust in the stratosphere. This will provide a basis for the companion paper which explores how the variations in the model transport affects the simulations of an HSCT perturbation.

2. GSFC-2D Model

The 2-D model at NASA/Goddard Space Flight Center (GSFC) was originally described in *Douglass et al.* [1989] and *Jackman et al.* [1990]. Recent improvements to the model have been discussed in *Jackman et al.* [1996], and upgrades to the transport formulation are described in *Fleming et al.* [1999]. Details of this new transport formulation are contained in the Appendix. We note that the bottom boundary condition used to compute the model residual circulation (equation A3 in the Appendix) is now more physically realistic than that used in recent assessment studies. This resulted in a somewhat slower stratospheric circulation and an older mean age of air than those published in the recent assessment reports [*Kawa et al.*, , 1999; *Park et al.*, 1999; *Hall et al.*, 1999].

We have updated the model reaction rates and photolysis cross sections to the latest Jet Propulsion Laboratory (JPL) 1997 recommendations [*DeMore et al.*, 1997]. We have also made some minor modifications to our model chemistry scheme. H_2O_2 is now transported, and the HO_x species ($H + OH + HO_2$) are now computed and transported using the family approach following *Douglass et al.* [1989]. The family members are computed from photochemical equilibrium and normalized to the total family concentration. In a similar fashion, the hydrocarbon products of CH_4 oxidation are now also computed as a family ($CH_x = CH_3 + CH_3O_2 + CH_3O + CH_2O + CH_3OOH$).

This replaces our previous methodology in which the individual HO_x and CH_x species were computed separately assuming photochemical equilibrium. This new formulation ensures that the total hydrogen and carbon atoms are conserved throughout the model run. However, we note that these changes did not impact on the model simulations shown in this study.

3. Results

We now show model simulations of several dynamical tracers from a variety of transport sensitivity tests, listed in Table 1. As discussed in *Fleming et al.* [1999], simulations with the base line model transport give the best overall comparisons with tracer observations. In the experiments shown here, we will illustrate how moderate and large changes away from this baseline transport affect the model simulations of long lived tracers. We will discuss how changes in the circulation, K_{yy}, and K_{zz} fields affect the simulations separately, and then in various combinations. We will also compare the results from our latest 1999 model with those obtained using the previous 1995 version of our model transport.

3.1. Sensitivity to the circulation

We first examine the model sensitivity to changing the residual circulation throughout the troposphere and lower stratosphere (the K_{yy} and K_{zz} fields remain fixed). In these experiments, we have increased and then decreased the circulation strength away from the baseline by moderate and then large amounts in the region below 35 km. These are defined as scenarios B, C, D, and E as listed in Table 1.

Figure 1 shows observations of ^{14}C at 31°N for July 1964 and July 1966, along with time dependent model simulations for the base transport (scenario A) and the four circulation sensitivity scenarios. The profiles for July 1964 correspond to 9 months after initialization. Both the observed and simulated peaks in ^{14}C at 20-25 km are

still fairly robust, with a strong decrease with height into the middle stratosphere. The weakest circulation gives the largest ^{14}C concentrations below the peak, with the strongest circulation producing the largest ^{14}C above 28 km during this time. Here the concentrations are directly related to the strength of the circulation which transports ^{14}C up from the source region near 20 km. Also, all of the circulation scenarios simulate larger than observed ^{14}C concentrations above ~26 km during this time. By July 1966 (2 years and 9 months after inialization), the maximum has been dissipated with very little vertical gradient seen above 22 km in the simulations and observations. At this time, removal of ^{14}C from the stratosphere is proportional to the circulation strength so that more ^{14}C is maintained in the stratosphere with a weaker circulation, similar to the findings of *Jackman et al.* [1991]. Qualitatively similar results are seen in simulations of strontium 90 (not shown) in the tropics and SH midlatitudes.

The annually averaged mean age of air derived from SF_6 for the baseline and 4 circulation scenarios (B, C, D, and E) is shown in Figure 2. In this study we use the global mean SF_6 time series at the surface [*Geller et al.*, 1997] as the reference for computing Γ in the stratosphere. The shapes of the contours in Figure 2 are typical of a long lived tracer illustrating the Brewer-Dobson circulation, with rising motion in the tropical stratosphere and descent in the extratropics. The age throughout the stratosphere becomes progressively older with a weaker circulation, although the general shapes of the age contours do not change appreciably with circulation strength. Ages of greater than 9 years are simulated in the upper stratosphere with the weakest circulation. This age dependence on the circulation strength is also illustrated in Table 1 which lists the annual/global average Γ at 19, 27, and 35 km for each transport scenario.

Figure 3 shows the mean age of air at 20 km for Oct/Nov 1994 derived from ER-2 SF_6 data taken from the Airborne Chromatograph for Atmospheric Trace Species (ACATS) instrument [*Elkins et al.*, 1996], along with the different model circulation scenarios. Figure 4 shows vertical profiles of the mean age at low, middle, and high

latitudes from the model simulations and ballon SF_6 observations of *Harnisch et al.* [1996] (asterisks) and the Observations of the Middle Stratosphere (OMS) campaign Lightweight Airborne Chromatography Experiment (LACE) instrument (F.L. Moore et al., manuscript in preparation, 1999) (triangles). Note that mean ages derived from CO_2 measurements [e.g., *Andrews et al.*, 1999] were found to be similar to those derived from SF_6 data at 20 km [*Hall et al.*, 1999].

Figures 3 and 4 again show that increasing the circulation strength decreases the stratospheric Γ everywhere above 15 km. The age differences between the different circulations are largest at the highest altitudes, with a ~6 year difference at 35 km between the very weak and very strong circulations. The overall vertical gradients and the latitudinal gradients between the tropics and mid-latitudes also decrease with increasing circulation strength. This shows that such gradients can be modified by the residual circulation as well as the horizontal diffusion rates. Note also that the dependence of the vertical age gradients on the circulation and the overall vertical structure of the midlatitude age distribution is very similar to that seen in the July 1966 ^{14}C simulation at 31°N in Figure 1.

Figures 1-4 illustrate the range of results that are obtained with the various circulation strengths, and how these compare against observations. While the baseline transport provides the best overall model-data comparison, both the moderately weak and moderately strong circulations (scenarios C and D) are within reasonable agreement with the observations in some of the comparisons. For example at 20 km in the tropics, the base and strong circulations compare well with the data, whereas the weak circulation indicates ages that are too old. However, the weak circulation is within the range of observations at 65°N in Figure 4, and provides the best agreement above 23 km with the OMS midlatitude data (triangles, middle panel). However, the base model agrees best with the midlatitude data of *Harnisch et al.* [1996] (asterisks). We note that the two midlatitude data sources show age differences of about 1 year in the

middle stratosphere, even though they are for similar latitudes and seasons. Some of this difference may be due interannual dynamical variability since the data were taken during different years (1996 versus 1993). Such variability is not accounted for in the model simulations.

It appears that the very weak and very strong circulations (scenarios B and E) produce ages that are outside the range of observations, and in some cases, far outside this range. An exception to this is the 65°N profile in which there are a few measurements of very old air (7-9 years) at 20-25 km thought to be remnants of the polar vortex [*Ray et al.,* 1999]. Such phenomena cannot be resolved by a zonal mean model, except with an artificially very weak circulation as shown in Figure 4. We note that it is possible that such observations of old ages are an artifact, in part, of a mesospheric photochemical loss of SF_6 [e.g., *Hall and Waugh*, 1998] which would be reflected in polar vortex air.

As a final transport diagnostic, Figure 5 shows vertical profiles of CO_2 plotted against N_2O in the SH polar vortex region from the ER-2 measurements [*Boering et al.,* 1996; *Andrews et al.,* 1999] and the model simulations. The CO_2-N_2O relationship in the stratosphere has been discussed previously [*Boering et al.,* 1996; *Strahan et al.,* 1998]. The tropospheric source of CO_2 has a secular trend along with a strong seasonal cycle in the NH. The source of N_2O is seasonally invariant and undergoes only a small secular increase. At high southern latitudes where the CO_2 seasonal amplitude in the lower stratosphere is quite small, it would be expected that variations in CO_2 for a given value of N_2O will be due, in part, to the transport of the differing trends of the CO_2 and N_2O sources. Also, N_2O undergoes photochemical loss in the upper stratosphere which partially offsets the N_2O increase caused by a stronger circulation and larger mass flux from the tropical troposphere. CO_2 has no photochemical sink in the stratosphere so that it will be much more sensitive to transport changes compared to N_2O.

Figure 5 is representative of most latitudes and seasons. This shows that the

$CO_2 - N_2O$ correlation is strongly sensitive to the circulation such that for a given value of N_2O, CO_2 increases with an increasingly stronger circulation. With a very weak circulation, the vertical (and horizontal) gradients in CO_2 are significantly stronger relative to the baseline case. These gradients become weaker with increasing circulation so that with the very strong circulation, CO_2 is transported rapidly enough throughout the stratosphere to produce little or no horizontal or vertical gradients. Figure 5 illustrates that the base transport shows the best overall consistency with the data, with the other circulations being fairly far outside of the range of data, at least above N_2O levels of 275 ppbv. Below this level, the strong and very strong circulations (scenarios D and E) provide a better comparison with the data. However, incomplete resolution of processes near the tropopause in the model and/or localized effects in the data could also affect the model-measurement comparison in this region.

Given that CO_2 acts as a conserved tracer in the stratosphere and has a linear increase at the ground, Figure 5 can also be thought of as a vertical profile of the mean age. Since the seasonal cycle amplitude in CO_2 is quite small at high SH latitudes, the profiles in Figure 5 reflect the fact that the linear trend in the CO_2 source is transported through the stratosphere more rapidly with a stronger circulation. For example at the lowest N_2O values of 125 ppbv (corresponding to 22-25 km), the very weak and very strong circulations show a CO_2 difference of 8.6 ppmv. Assuming a linear increase in CO_2 of 1.4-1.5 ppmv/yr at the ground, this corresponds to an age difference of 5.7-6.1 years between the very weak and very strong circulations. This is consistent with the differences in Γ derived from SF_6 in the SH polar lower stratosphere shown in Figure 2.

3.2. Sensitivity to lower stratospheric K_{zz}

Observational studies [e.g., *Hall and Waugh*, 1997; *Mote et al.*, 1998], have shown that the vertical diffusion (K_{zz}) in the lower tropical stratosphere is .01-.02 m^2/s, and we have adopted this value in our base model simulation. In this section, we investigate

the sensitivity to changing the K_{zz} values in the lower stratosphere away from this baseline value.

Figure 6 shows the model simulations of ^{14}C in July 1966 for minimum lower stratospheric K_{zz} values of 0.001, 0.1, and 1 m^2/s (scenarios F, G, and H). Also plotted here are the base model scenario A and observations identical to Figure 1. We found that using a minimum stratospheric K_{zz} smaller than 0.001 m^2/s does not change the model response in the diagnostic tracers so that this value appears to be the lower limit of K_{zz} in our model. These scenarios are consistent with the circulation changes in Figure 1 in that a slower (faster) transport maintains more (less) ^{14}C throughout most of the stratosphere. Values of K_{zz} between 0.001 and 0.1 m^2/s cause relatively small changes in the ^{14}C simulation above 18 km, with the baseline or K_{zz} value of 0.1 m^2/s providing reasonable agreement with the data. There is very little difference among scenarios A, F, and G below 18 km, with all 3 providing good agreement with the data. Using a K_{zz} of 1 m^2/s (scenario H) causes mixing within and removal of material from the stratosphere that is much too rapid. This results in simulations that are far outside the range of observations as seen in Figure 6.

The annually averaged mean age distributions for the baseline and K_{zz} scenarios are shown Figure 7. Figures 8 and 9 show the latitudinal and vertical profiles of mean age for these simulations, along with the base case and observations as in Figures 3 and 4. Similar to the circulation changes, Γ throughout the stratosphere becomes progressively younger with increasing K_{zz}. Using a minimum K_{zz} beween 0.001 and 0.1 m^2/s varies the age of air by at most 1 year, but the resulting simulations are within the range of observations. An exception to this is the vertical profile at midlatitudes where the smallest K_{zz} agrees quite well with the Harnisch *et al.* [1996] profile, but is still $\sim$ 1 year too young above 23 km compared to the OMS data. Similar to the circulation changes, the latitudinal and vertical age gradients decrease with increasing K_{zz}.

Consistent with the ^{14}C simulations, using the very large K_{zz} of 1 m^2/s (scenario H)

simulates ages that are much too young everywhere, and gives latitudinal and vertical gradients in Γ that are much weaker than observed. The simulations with this large K_{zz} are consistent with the model-measurement intercomparison analysis of *Hall et al.* [1999] who concluded that a K_{zz} of 1 m^2/s is unrealistic and that 0.1 m^2/s is close to the expected upper limit on K_{zz}. We note also that this tracer dependence on K_{zz} is similarly seen in the simulated $CO_2 - N_2O$ relationship (not shown).

3.3. Sensitivity to mesospheric gravity wave effects

The model gravity wave parameterization computes diffusion, used as the model mesospheric K_{zz} field, and wave drag which has a direct effect on the model residual circulation (see Appendix). The relative importance of vertical diffusion and vertical advection by the residual circulation in controlling the water vapor distribution in the mesosphere has been debated previously [e.g., *Garcia and Solomon*, 1985; *Holton and Schoeberl*, 1988; *Smith and Brasseur*, 1991; *Nedoluha et al.*, 1996]. Figure 10 shows the seasonal variation in H_2O at 80 km as measured by the Halogen Occultation Experiment (HALOE - version 19) instrument onboard the the Upper Atmosphere Research Satellite (UARS). In our model, vertical advection is the dominant process controlling H_2O throughout most of the mesosphere, and is largely responsible for the H_2O seasonal cycle [*Chandra et al.*, 1997]. Figure 10 shows that the base model scenario resolves the overall seasonal cycle seen in the HALOE data reasonably well.

Vertical diffusion, which maximizes during the solstice seasons when the westerly and easterly midlatitude jets are strongest, plays a secondary role in determining the extratropical H_2O seasonal variations in our model. This diffusion acts to increase (decrease) H_2O in the upper (lower) mesosphere. In the upper mesosphere, the diffusive transport therefore enhances the advectively-driven water vapor increase in summer. Conversely, diffusion partially offsets the advectively-induced H_2O decrease in winter. These effects maximize at 80 km, resulting in secondary maxima during mid-winter at

midlatitudes. This effect is somewhat more pronounced in the SH winter because the stronger zonal westerlies, and hence the larger difference between the background zonal wind and the gravity wave phase speed, allow for larger diffusion compared to the NH winter. These secondary mid-winter maxima are seen in the HALOE data in Figure 10, and it appears that our model captures these features reasonably well, including the larger secondary maximum in the SH. We note that horizontal advection by the residual circulation has a substantially smaller influence on mesospheric H_2O compared to either the vertical advection or vertical diffusion.

To test how these processes affect tracers in the stratosphere, we ran two additional scenarios with weak and strong mesospheric gravity wave-induced drag, which affects the circulation, and diffusion, relative to the base case (scenarios I and J). As seen in Figure 10, these scenarios have a large effect on mesospheric H_2O. Stronger gravity wave effects lead to larger water concentrations at 80 km due to the net effect of increasing the upward transport of H_2O from the stratosphere. The base model gives the most favorable overall comparison with the HALOE data, especially at midlatitudes. The strong gravity wave scenario (J) also shows some reasonable agreement, especially at the equator. However, the weak gravity wave case (I) simulates very small mesospheric H_2O, especially in the winter extratropics, and compares rather poorly with the HALOE data.

Despite the large induced changes in the mesosphere, these scenarios exert very little influence on tracer distributions in the lower and middle stratosphere in our model. The changes in global and annual mean age below 35 km between scenarios I and J and the base case were at most 4-5 months (Table 1). Furthermore, only very small changes were seen in the model simulations of ^{14}C below 35 km.

3.4. Sensitivity to stratospheric K_{yy}

Figure 11 shows distributions of mean age for several different K_{yy} scenarios

along with the baseline model. Here we have decreased and increased the K_{yy} values everywhere above the tropopause by constant factors of 2 and 5 (scenarios K, L, M, and N in Table 1). As expected, the latitudinal gradients in Γ become progressively weaker with increasing horizontal diffusion. It is also apparent that the mean age throughout the stratosphere above 16 km becomes increasingly older with increasing K_{yy} (see also Table 1). This is due to the fact that with larger K_{yy}, air parcels undergo more recycling through the middle atmosphere via ascent in the tropics and descent in the extratropics, before returning to the troposphere, and hence achieve an older mean age [e.g., *Bacmeister et al.,* 1998; *Hall et al.,* 1999]. Ages greater than 12 years are simulated in the upper stratosphere for the largest K_{yy} case (scenario N, Figure 11b).

The rate of horizontal mixing between the tropics and midlatitudes has been examined in previous studies [e.g., *Plumb,* 1996]. Our base model tropical-subtropical K_{yy} field varies spatially and seasonally, ranging from 10^8 to 10^{10}cm^2/s (see Appendix). The very large K_{yy} scenario (N) includes large K_{yy} throughout the tropics and is akin to the "global diffuser" model discussed by *Plumb,* [1996]. To further test the tracer sensitivity to our model horizontal diffusion across the tropics, we ran an additional scenario (Q) in which K_{yy} was set to a very small value of 10^8cm^2/s throughout the tropical stratosphere (15°S-15°N, 15-50 km) for all seasons. This is similar to the "tropical pipe" model of *Plumb,* [1996]. The resulting mean age contours in Figure 11f show very large horizontal gradients between the tropics and midlatitudes reflecting a very isolated tropical region. Γ is younger throughout the stratosphere in this case, with differences of almost 2 years in the high latitude middle stratosphere relative to the base case. Note also the small isolated region of $\Gamma > 5$ years in the very lower stratosphere over the Antarctic.

Latitudinal variations of Γ for these K_{yy} scenarios are shown in Figure 12 which again illustrates the general increase in mean age with increasing K_{yy}. At this level, it appears that the simulation is in reasonable agreement with the observations for

moderate changes in eddy diffusion. Even the smallest K_{yy} case (scenario K) shows some agreement with the data at midlatitudes. However, the largest K_{yy} case simulated Γ that is much older than observed at almost all latitudes. At 20 km, the small tropical K_{yy} scenario (Q) simulates ages in the tropics that are almost 1 year younger relative to the base case, due to the lack of in-mixing of older midlatitude air. The corresponding subtropical gradient is much stronger in this case, with slightly younger ages again simulated at high latitudes relative to the base case.

The vertical profiles in Figure 13 show the strong K_{yy}-age dependence above 20 km which is similarly seen in $CO_2 - N_2O$ profiles (not shown). The extreme scenarios (K and N) appear to be far outside the range of data above about 25 km. At midlatitudes, the base model agrees with the Harnisch *et al.,* data, while the moderately large case (scenario M) agrees best with OMS data. A similar finding was seen in the circulation tests in section 3.1. The vertical gradient in Γ above 20 km also shows a strong dependence on horizontal diffusion such with the gradient weakens with a progressively smaller global K_{yy}. At middle and high (not shown) latitudes, the vertical gradient is very close to zero for the smallest K_{yy} case. This illustrates the dominance of the residual circulation, which is primarily downward in this region, in controlling the long lived tracer distributions in this case. We note that Γ from the small tropical K_{yy} scenario (Q) (not shown in Figure 13) is nearly identical to the $K_{yy}/2$ case (scenario L) at these latitudes. As the recycling of air throughout the stratosphere is inhibited in the reduced tropical K_{yy} case, Γ at all latitudes above 20 km is decreased. Mean ages are younger by as much as 1.5 years at 35 km at 65°N relative to the base case.

Thus far, we have treated changes in K_{yy} separately from other changes in the model transport. However in reality, changes in K_{yy} are due to changes in wave driving which simultaneously affect the residual circulation. To investigate this coupling, we ran an additional scenario in which K_{yy} has been decreased by a factor of 5 as in scenario K, along with a corresponding factor of 5 decrease in the wave drive (also above the

tropopause), which weakens the circulation. We also ran a case in which both K_{yy} and wave drive were increased by a factor of 5. These are listed as scenarios O and P in Table 1.

The age of air response to increasing or decreasing K_{yy} and wave drive self-consistently is illustrated in Figures 11g-h. In these cases, the shapes of the contours are similar to those in which only K_{yy} has been changed (Figures 11a-b). However, additionally reducing the wave driven circulation increases the age everywhere, and produces isolated regions of old air in the high latitude lower stratosphere in both hemispheres. Conversely, increasing the circulation together with the K_{yy} field in Figure 11h drastically reduces the mean age throughout the stratosphere.

Latitudinal profiles of these scenarios at 20 km are shown in Figure 14. Again, decreasing only K_{yy} (dashed-triple dotted line identical to Figure 12) results in younger ages everywhere compared to the base case. As discussed in section 3.1, slowing the circulation produces older ages throughout the stratosphere. The net effect of including both the weaker wave driven circulation and K_{yy} (dashed-single dotted line in Figure 14) produces younger air in the tropics, older air in the extratropics, and a stronger subtropical age gradient, relative to the base case.

Figure 14 also shows the dramatic increase in Γ throughout the stratosphere obtained by increasing K_{yy} (dotted line, identical to Figure 12). However, increasing both K_{yy} and the wave drive (dashed line) has the opposite effect, with the mean ages being much younger everywhere and the age gradients being much weaker compared to either the base scenario or the observations. Note that because of the small inherent wave drive in the tropical stratosphere, decreasing this quantity in the tropics to be dynamically consistent with the very small K_{yy} used in scenario Q gave virtually the same mean age response compared to decreasing K_{yy} only.

We note that the combined K_{yy} and wave drive changes shown here are a somewhat incomplete representation of the true atmosphere. In reality, changes in K_{yy} and the

wave driven circulation would also change $\bar{T}$, the diabatic heating rates, and the $\bar{u}$ structure, which in turn will affect the wave propagation charcteristics responsible for the changes in K_{yy} and wave drive. Quantifying such changes in a completely consistent manner is difficult in our model given the empirical nature of the transport fields. To be fully self-consistent would require using an interactive chemical-radiative-dynamical 2-D model, such as reported in *Bacmeister et al.* [1998].

As a final K_{yy} sensitivity test, we investigated the model response to changes in horizontal diffusion across the tropopause. Recent reports have noted the importance of cross-tropopause transport in model simulations of HSCT emissions [e.g., *Park et al.*, 1999]. It was suggested that 2-D and 3-D models simulate a different correlation between mean age and NO_y accumulation, perhaps because of the inherent differences between 2-D and 3-D model formulations of cross-tropopause transport, which can have large zonal asymmetries. In our 2-D model, the tropopause, which is a function of latitude and season and is based on NCEP data, separates very fast and very slow vertical mixing (K_{zz}) regimes. There is also cross-tropopause transport horizontally via the K_{yy} field where the tropopause height changes with latitude. This occurs primarily at midlatitudes between $\pm 25^{\circ} - 60^{\circ}$. To test how this horizontal transport affects the diagnostic tracer simulations, we ran an additional model scenario (R) in which the cross-tropopause K_{yy} values were significantly increased over the baseline case (the K_{zz} values remain unchanged). In this case, simulations of long lived tracers were nearly identical to the baseline case. Mean ages were at most 2 months older throughout the stratosphere in scenario R compared to the base case (Table 1). As shown in the companion paper, the $\Gamma - NO_y$ correlation also changed only very slightly in this case. This illustrates the very small tracer sensitivity to the rate of horizontal cross-tropopause transport in our model simulations.

3.5. Sensitivity to combined transport changes

In this section we explore how simultaneous changes to the circulation, K_{yy}, and K_{zz} fields affect the long lived tracer simulations. Scenario S combines transport changes which all contribute to a moderately long stratospheric residence time, as reflected in the mean age in Figures 15a, 16 and 17 (see also Table 1). These include the weak circulation (scenario C), small lower stratospheric K_{zz} (scenario F), and moderately large K_{yy} (scenario M). This scenario gives very old ages of greater than 12 years in the upper stratosphere and mesosphere, with a strong vertical age gradient in the lower stratosphere (Figure 17, dashed-triple dotted line). Although the latitudinal age gradients in the middle and upper stratosphere are generally weaker than the base case due to the larger K_{yy}, the gradients are actually a bit stronger in scenario S in the lower stratosphere (Figure 16).

Scenario T combines the transport changes which contribute to a moderately short stratospheric residence time. These include the strong circulation (scenario D), moderately large K_{zz} (scenario G), and moderately small K_{yy} (scenario L). The young ages produced by this scenario are seen in Figure 15b, along with weaker latitudinal gradients in the lower stratosphere (Figure 16, dotted line) and weaker vertical gradients throughout the stratosphere (Figure 17, dotted line). Figures 16 and 17 show that at levels above the very lower stratosphere, both scenarios S and T give tracer simulations that are significantly different from the observations.

To test the extreme limits of these sensitivity tests, we combined the transport scenarios which had the very longest and very shortest stratospheric residence times discussed in this study. Scenario U combines the very weak circulation (scenario B), small K_{zz} (scenario F), and very large K_{yy} (scenario N), with the opposite combination (scenarios E, H, and K) used for scenario V. As shown in Figures 15c-d and in Table 1, mean ages in the middle stratosphere are > 20 years for scenario U and < 2.5 years for scenario V. These simulations are even further outside the range of measurements than

those given by scenarios S and T in Figures 16-17. These cases represent the absolute extremes of stratospheric mean age and residence time that we obtained in this study by varying the advective and diffusive transport rates in our model.

3.6. 1995 model transport

As a final scenario, we ran the tracer imulations using the previous 1995 version of our model transport (scenario W). This version of the model was used in the 1995 NASA HSCT assessment [*Stolarski et al.,* 1995] As seen in Figures 16-17, the new 1999 model transport (base scenario A) simulates tracers that are in significantly better agreement with observations compared to the previous 1995 transport [see also *Fleming et al.,* 1999]. The contour shapes of Γ are also significantly different between the 1999 and 1995 models (Figures 15e-f), with the 1995 model simulating greater asymmetry between the hemispheres and weaker gradients overall than the 1999 model. Furthermore, the gradients and absolute values of ^{14}C and mean age in the 1995 model are significantly underestimated, relative to observations, indicating that the transport rates are too fast in this older model version. The simulated annual/global mean ages are 40-60% younger throughout the stratosphere compared with the 1999 model transport. The 1995 model simulations in Figures 16-17 are actually similar to those of the combination short residence time scenario (T).

There are substantial differences between our 1999 and 1995 model transport formulations which are reflected in these simulations. While there have been changes to the mean circulation, much of the differences are due to changes in the meridional and vertical diffusive transport. The 1999 model is generally less diffusive in a globally averaged sense, and exhibits greater isolation between the troposphere and stratosphere, i.e., a sharper change in K_{zz} across the tropopause. There is also a sharper transition in K_{yy}, and hence greater isolation, between the tropics, subtropics, and midlatitudes in the stratosphere in the 1999 model.

3.7. Chemically active tracers

Previous studies have examined how transport variations affect tracers that are chemically active [e.g., *Hall et al.*, 1999; *Schoeberl et al.*, 1999; *Li and Waugh*, 1999]. Because of the rapid photochemical time scales in the upper stratosphere, constituents such as N_2O and Cl_y are less dependent on transport rates compared to inert tracers such as SF_6. Therefore, chemically active tracers can hide model transport changes and hence, transport deficiencies. Figure 18 shows the global and annually averaged Cl_y and N_2O concentrations at 27 km plotted against mean age for the 23 transport scenarios discussed in this study. This level is characteristic of other stratospheric altitudes and shows a strong correlation of mean age with both Cl_y and N_2O. Faster transport rates result in younger ages, and yield smaller concentrations of Cl_y (less conversion of inorganic chlorine to Cl_y), and larger N_2O values (less photochemical destruction). The base scenario (depicted by the large letter "A" in Figure 18) appears near the middle of the different transport scenarios.

Figure 18 also shows that the correlation pattern is not linear, but rather shows an asymptotic behavior. This is consistent with previous studies [e.g., *Hall et al.*, 1999; *Schoeberl et al.*, 1999; *Li and Waugh*, 1999], suggesting that very slow transport rates which give long stratospheric residence times strongly affects inert tracers such as Γ. However, photochemically active species such as N_2O and Cl_y show progressively less sensitivity to decreasing transport rates, since most if not all of the N_2O has been photochemically destroyed, and the inorganic chlorine converted to Cl_y in very old air.

The response of chemically active tracers to the stratospheric residence time, or lifetime, is also seen in Figure 19. Here we plot the correlation of mean age with the stratospheric steady state lifetimes of $CFCl_3$ and N_2O for the different transport scenarios (see also Table 1). Recently, *Volk et al.* [1997] estimated the lifetimes of several source gases using ER-2 aircraft observations, and found significantly shorter lifetimes compared to those derived from 2-D model calculations [e.g., *WMO*, 1995]. The *Volk et*

al. [1997] best estimate of the lifetimes of $CFCl_3$ and N_2O, along with the 1 standard deviation uncertainties, are plotted with our model results in Figure 19.

As in Figure 18, the model simulations show a strong correlation between mean age and the $CFCl_3$ and N_2O lifetimes. With faster transport rates there is a larger constituent concentration in the stratosphere, but a greater increase in the constituent loss rates compared to the base case, so that the net effect is to decrease the lifetime. The correlation with mean age is almost completely linear for these tracers. Our base scenario reveals a stratospherically averaged (pressure weighted) mean age of 2.9 years, with lifetimes for $CFCl_3$ and N_2O of 68 and 136 years, respectively. Scenario V simulates the shortest stratospheric residence time and youngest mean age, with lifetimes of 77 years for N_2O and 27 years for $CFCl_3$. Conversely, the longest residence time and oldest Γ is simulated by scenario U, which gives lifetimes for N_2O and $CFCl_3$ of 461 years and 231 years, respectively.

The majority of our model transport scenarios simulate N_2O lifetimes that are within the range of the *Volk et al.* [1997] estimates (98-146 years). These include several scenarios with very fast transport rates, e.g., the very strong circulation (E) and fast stratospheric vertical mixing (H), even though the mean age and ^{14}C distributions for these scenarios were far outside the observational range. The base scenario N_2O lifetime is somewhat longer than the best empirical estimate, but is still within the range of observations. For the $CFCl_3$ lifetimes, only the rather short residence time scenarios are within the range of the Volk *et al.* estimates, and the base scenario $CFCl_3$ lifetime of 68 years is ~50% longer than the observations. Scenarios with very long residence times, e.g. the very weak circulation (B), fast horizontal mixing (N), and the combination scenarios S and U, revealed lifetimes for both N_2O and $CFCl_3$ that are much longer than observed. Interestingly, the 1995 model transport (scenario W) appears to give the best overall agreement with the observations for both the N_2O and $CFCl_3$ lifetimes. However as seen in Figures 16-17, this scenario gave significantly poorer agreement with

other tracer observations compared to the base 1999 transport scenario (A).

4. Conclusions

In this study, we have examined the effects on stratospheric long lived tracers of relatively moderate and large changes to the base transport fields in our 2-D model. Changes to the strength of the residual circulation in the upper troposphere and stratosphere had an effect similar to changing the lower stratospheric K_{zz} values: increasing the transport rates decreased the overall stratospheric residence time, and hence the mean age, and increased the rate of removal of material from the stratosphere.

Increasing the stratospheric horizontal diffusion decreased the latitudinal tracer gradients, but increased the overall stratospheric mean age. This is due to the fact that with a larger K_{yy}, air parcels undergo more recycling through the middle atmosphere via ascent in the tropics and descent in the extratropics, before returning to the troposphere. Simulations with very small tropical stratospheric K_{yy} resulted in a very isolated tropical region and reduced the mean age throughout the stratosphere, with Γ younger by as much as 25% in the mid-upper stratosphere. Also, large scale reductions in K_{yy} strongly reduced the *vertical* gradients in Γ above 20 km in the extratropics, illustrating the dominance of the residual circulation in controlling the long lived tracer distributions with relatively small global K_{yy} values.

We found that significant variations in the strength of the mesospheric gravity wave drag and diffusion strongly influenced the simulated seasonal cycle of water vapor in the upper mesosphere, but caused only very minor changes to ^{14}C and the mean age below 35 km. Similarly, the model simulations in the stratosphere showed only very small sensitivity to the magnitude of the horizontal diffusive transport across the tropopause.

Incorporating K_{yy} changes along with self-consistent changes in the corresponding planetary wave drive, and hence, the residual circulation, had a cancellation effect, and produced significantly different tracer simulations compared to changing only the K_{yy}

rates. While increasing K_{yy} globally increases the mean age, a stronger wave drive, and hence, an enhanced circulation implied by a larger K_{yy} acts to decrease the mean age, with the net effect giving significantly younger ages everywhere relative to the base case. The shortest stratospheric residence time and youngest mean age obtained in this study were simulated by combining a strong circulation, large K_{zz}, and small K_{yy} field. Conversely, combining a weak circulation, small lower stratospheric K_{zz}, and a large stratospheric K_{yy} field yielded the longest stratospheric residence time and oldest mean age. The upper and lower limits of the annual/globally averaged middle stratospheric Γ obtained in this study ranged from $\sim$1 year to slightly more than 20 years.

The model simulations revealed a strong correlation between mean age and chemically active tracers, both in concentration and calculated lifetimes. The correlation between Γ and both N_2O and Cl_y concentrations showed an asymptotic behavior. This is indicative of the fact that as transport rates decrease and stratospheric residence times and mean age increase, N_2O and Cl_y, which are photochemically active, become progressively less sensitive to transport.

The base model transport provided the most favorable overall comparison with a variety of observations, and represents a significant improvement over our 1995 transport formulation. Moderate changes to the base transport were found to provide modest agreement with some of the measurements. Scenarios with residence times ranging from moderately shorter to slightly longer relative to the base case simulated N_2O lifetimes that were within the observational estimates of *Volk et al.* [1997]. However, only scenarios with rather fast transport rates were comparable with the Volk *et al.* estimates of $CFCl_3$ lifetimes. This is inconsistent with model-measurement comparisons of mean age in which the base model or scenarios with transport rates slightly slower than the base case compared the most favorably with balloon SF_6 data. We also found that large transport changes away from the base case resulted in simulations that were outside the range of measurements, and in many cases, far outside this range.

Finally,

These transport scenarios can be used to explore the sensitivity to dynamics of model simulations of an HSCT perturbation. This will be addressed in part 2 of this study.

Appendix: GSFC 2-D Model Transport Description

Earlier versions of the model transport derived the residual circulation $(\bar{v}^*, \bar{w}^*)$ using climatological temperatures and heating rates in the TEM thermodynamic and continuity equations [e.g., *Dunkerton*, 1978]. The planetary wave-induced K_{yy} distribution was determined self-consistently from the circulation using the residual needed to balance the zonal momentum equation [*Newman et al.*, 1988]. A simple, weakly height-varying K_{zz} field with no latitudinal or seasonal variations was used to describe turbulent diffusion induced by gravity wave breaking in the mesosphere. These dynamical fields were able to capture some general features seen in long-lived tracer observations. However, this transport did not explicitly include planetary or gravity wave effects. Therefore, many details of the observed zonal mean transport were not resolved in the model simulated tracer fields.

We have upgraded the model transport formulation which now generally follows that of interactive 2-D models [*Garcia and Solomon*, 1983]. However, the new dynamical fields are based on empirical data sets as opposed to being computed interactively in the model. This scheme uses explicit diagnostic calculations of planetary and synoptic scale wave effects, along with parameterizations to account for gravity wave and Kelvin wave effects in which the zonal mean flow is constrained to observations. Compared to our previous methodologies, this new formulation provides an improved representation of the zonal mean dynamics [*Fleming et al.*, 1999]. As with previous model versions, the transport is climatological and does not account for the quasi-biennial oscillation or other interannual variability. Details of the new formulation are described below.

A.1. Zonal Mean Formulation

Following the methodology originally outlined in *Garcia and Solomon* [1983], the TEM residual circulation $(\bar{v}^*, \bar{w}^*)$ is computed from the meridional streamfunction $(\bar{\chi}^*)$.

An elliptic equation for $\bar{\chi}^*$ is obtained from the zonal mean momentum, thermodynamic, thermal wind, and continuity equations of the TEM system [e.g., *Andrews et al.*, 1987],

$$C_{zz}\frac{\partial^2\bar{\chi}^*}{\partial z^2} + C_z\frac{\partial\bar{\chi}^*}{\partial z} + C_{zy}\frac{\partial^2\bar{\chi}^*}{\partial y\partial z} + C_y\frac{\partial\bar{\chi}^*}{\partial y} + C_{yy}\frac{\partial^2\bar{\chi}^*}{\partial y^2} + C_0\bar{\chi}^* = C_F\cos\phi \qquad \text{(A1)}$$

The coefficients ($C_{zz}, C_z, C_{zy}, C_y, C_{yy}$, and C_0) depend on empirically determined $\bar{u}$ and $\bar{T}$ fields (discussed below) and are similar to those derived in *Garcia and Solomon* [1983]. The forcing term (C_F) is proportional to the vertical gradient of the total momentum forcing and the latitudinal gradient of the total heating rate,

$$C_F = f_1\frac{\partial}{\partial z}(F_{PW} + F_{GW} + F_{KW}) + \frac{R}{H}\frac{\partial}{a\partial\phi}(Q_D + Q_L + Q_{GW} + Q_{PW}) \qquad \text{(A2)}$$

Here, mechanical forcing is taken as the E-P flux divergence due to dissipating planetary waves (F_{PW}), gravity waves (F_{GW}), and equatorial Kelvin waves (F_{KW}). Thermal forcing is due to the combined effects of the net diabatic heating (Q_D), latent heating (Q_L), and the net eddy heat flux associated with planetary waves (Q_{PW}) and gravity wave breaking in the mesosphere (Q_{GW}). These quantities will be described in the following sections.

This methodology allows us allows us to compute the planetary wave momentum forcing (F_{PW} in equation A1) and self-consistent K_{yy} fields directly from 3-D meterological analyses, instead of inferred from the residual in the momentum equation. This approach differs from previous diagnostic calculations which compute the residual circulation from only the thermodynamic and continuity equations [e.g., *Shine,* 1989; *Eluszkiewicz et al.,* 1996].

The $\bar{u}$ and $\bar{T}$ fields used in the coefficients in equation (A1) were compiled primarily from the 17-year (1979-1995) average of NCEP data for 1000-1 mbar, and the CIRA-86 empirical reference atmosphere [*Fleming et al.,* 1990] for the mesosphere above 1

mbar. In most regions outside the tropics, zonal mean winds were derived from the temperatures [*Fleming et al.,* 1990]. At low latitudes (±20°) where the thermal wind derivation is problematic, and at all latitudes above 80 km where the temperature data contained in the CIRA model is sparse, we used climatological zonal wind measurements from the high resolution Doppler imager (HRDI) onboard UARS. Below 10 km where HRDI does not make measurements, zonal wind at 20°S-20°N was derived from a second derivative thermal wind calculation [*Fleming et al.,* 1990]. The temperature and zonal wind fields were adjusted where necessary to maintain exact thermal wind balance in all regions, as necessitated by the streamfunction formulation. Figure A.1a-b shows these fields for January and indicates the well known zonal mean structure during solstice conditions, as has been discussed frequently in previous climatological compilations [e.g., *Randel,* 1992; *Fleming et al.,* 1990].

To obtain $\bar{\chi}^*$, equation (A1) is solved from pole to pole in finite difference form by either successive over-relaxation or the method of *Lindzen and Kuo* [1969]. The altitude range extends from the ground to ~116 km. The model chemistry extends up to 90 km, and the 90-116 km layer has only an abbreviated representation of the dynamics and acts as a sponge layer for the model transport. For boundary conditions, $\bar{v}^*=0$ at the poles and $\bar{w}^*=0$ at the ground (1013 mbar) and the top boundary (0.00008 mbar) so that there is no flow into or out of the model domain ($\bar{\chi}^*=0$ at the four boundaries). The streamfunction formulation satisfies the condition, $\int_{-90^\circ}^{+90^\circ} \rho\bar{w}^* \cos\phi d\phi = 0$.

To obtain reasonable long lived tracer simulations in the stratosphere, it is necessary to impose an additional boundary condition on $\bar{\chi}^*$ at one level above the ground (762 mb - denoted as $\bar{\chi}_2^*$). Following *Garcia et al.* [1992], we calculate $\bar{\chi}_2^*$ as,

$$\bar{\chi}_2^* = -\frac{\cos\phi}{f\rho_2}\int_{z_2}^{\infty} \rho(F_{PW} + F_{GW} + F_{KW})dz \qquad \text{(A3)}$$

This expression is derived from the linearized steady state momentum equation,

$-f\bar{v}^* = F_{PW} + F_{GW} + F_{KW}$, and follows from the downward control principle under quasi-geostrophic scaling [e.g., *Haynes et al.,* 1991; *Rosenlof and Holton,* 1993]. Equation (A3) is applied poleward of 15°N (°S) with values in the tropics interpolated between ±15°. The vertical velocity at 762 mbar obtained from $\bar{\chi}_2{}^*$ depends solely on the momentum forcing of the free atmosphere above this pressure surface. Upward motion out of the boundary layer generally occurs equatorward of ±50° with downward motion into the boundary layer at higher latitudes. To obtain good model-measurement comparisons of total ozone and long lived tracers, we weakened the circulation by scaling the expression in (A3) by a constant factor of .75 for all latitudes and seasons. We note that as an independent check of this method, a very similar circulation was obtained by computing $\bar{\chi}_2{}^*$ via the definition, [e.g., *Andrews et al.,* 1987],

$$\bar{w}^* \equiv \bar{w} + \frac{1}{a\cos\phi}\frac{\partial}{\partial\phi}\left[\cos\phi\frac{\overline{v'T'}}{(\partial\bar{T}/\partial z + \kappa\bar{T}/H)}\right] \qquad \text{(A4)}$$

using climatological averages of the NCEP reanalyses [*Kalnay et al.,* 1996].

Figure A.1c-d shows $\bar{w}^*$ and $\bar{v}^*$ for January. These fields are generally similar to previous model calculations [e.g., *Garcia et al.,* 1992]. Upward motion is seen throughout the tropical stratosphere, and in the extratropical middle to upper stratosphere and mesosphere in summer. Maximum ascent of 3.6 cm/s occurs in the polar upper mesosphere. The winter extratropics are characterized by downward motion throughout the troposphere and middle atmosphere. The strong upward motion of the Hadley cell is also evident in the tropical troposphere. The meridional velocities are generally weak in the stratosphere, but reach maximum values of 6-7 m/s in the upper mesosphere reflecting the summer to winter meridional flow pattern induced by gravity wave drag (section A.3.b).

Figure A.2 shows a heuristic view of the model residual circulation, depicted by streamlines, and the simulated stratospheric CH_4 distribution shown in color, for

January and September. This illustrates the controlling influence of the circulation on long lived tracers such as CH_4. Upward motion is present in the tropical stratosphere throughout the year, advecting CH_4-rich air up from the troposphere. Strong descent is evident in the winter polar region of both hemispheres, which brings CH_4-poor air down from the mesosphere. The summer lower stratosphere in both hemispheres is characterized by very weak vertical motion.

A.2. Heating Rates

The latent heating rates (Q_L) are based on the empirical climatology compiled by *Newell et al.* [1974], shown in Figure A.3a. The diabatic heating rates (Q_D) are computed following *Rosenfield et al.* [1994], using climatological temperatures (section A.1), ozone, and water vapor. The ozone climatology was constructed as follows. Values in the troposphere are based on SBUV data as described in *McPeters et al.* [1984]. SAGE II data (both sunrise and sunset) for 1984-1989 are used in the lower stratosphere (100-10 mbar). Nimbus-7 SBUV data for 1979-1989 are used for the upper stratosphere (10-0.7 mbar), and SME IR and UV measurements for 1982-1986 are used for the mesosphere above 0.7 mbar. The water vapor climatology is based on *Oort* [1983] for the ground to 375 mbar, SAGE II data for the upper troposphere and stratosphere, and the reference profile of *Remsberg et al.* [1989] for the mesosphere above 1 mbar.

The net diabatic heating rates for January are shown in Figure A.3b. These values are generally consistent with previous heating rate calculations that utilize climatological data [e.g., *Shine*, 1989; *Huang and Smith*, 1991; *Newman and Rosenfield*, 1997]. Net diabatic heating (cooling) is seen in regions where the observed temperature is colder (warmer) than the radiative equilibrium temperature. Largest cooling occurs in the winter extratropics due to planetary and gravity wave effects, with the latter being dominant in the mesosphere. Gravity wave breaking drives the summer mesosphere to be far colder than the radiative equilibrium temperature, leading to large net diabatic

heating there. Small net diabatic cooling occurs throughout the troposphere during all seasons. Largest values are ~-1.5 K/day which occur in the tropical mid-troposphere.

Gravity wave breaking in the mesosphere induces a net thermal flux due to the combination of an eddy heat flux convergence and the turbulent diffusion of the mean thermal field. We account for the net heating due to these processes following *Schoeberl et al.* [1983] and *Huang and Smith* [1991]. Here we utilize the observed temperature climatology (section A.1) and vertical diffusivity computed from the gravity wave parameterization (section A.3.b). Our calculated net heating from these processes (Q_{GW}, Figure A.3c) is generally similar to that obtained in the previous studies. Net cooling occurs throughout almost the entire mesosphere, with a maximum of -12.5 K/day at 80-90 km in the mid-latitude SH during January.

Planetary waves also induce a net thermal flux (Q_{PW} in equation A2). This quantity (not shown) can be computed from 3-D meteorological fields [e.g., *Andrews et al.*, 1987], but is small compared to the other heating rate contributions. Maximum values are generally less than ±.75 K/day occurring in the high latitude winter stratosphere-lower mesosphere, and the mid-high latitude troposphere throughout the year.

The total heating rate for January is shown in Figure A.3d. Diabatic heating/cooling dominates the total throughout the stratosphere, with the gravity wave effects playing a significant role in the mesosphere along with the diabatic contribution. Both the diabatic and latent heating are important in the troposphere, and the combination of these processes leads to horizontal gradients in the total heating rate which determines the classical Hadley cell circulation in the tropical troposphere and lower stratosphere (Figure A.1c).

A.3. Wave Parameterizations

A.3.a. Planetary and Synoptic Scale Waves

Planetary wave dissipation generates rapid irreversible mixing of tracers which

can be expressed as a horizontal diffusive transport in two-dimensional models. This wave dissipation also induces a drag on the zonal mean flow which can modify the mean advective transport by the meridional circulation. Previous investigations have illustrated the importance of accounting for these processes in a self-consistent manner [*Newman et al.*, 1988; *Garcia*, 1991].

The E-P flux divergence computed from 3-dimensional meteorological analyses [e.g., *Andrews et al.*, 1987] provides a diagnostic estimate of the planetary wave drag (F_{PW} in equation A2). Following *Randel and Garcia* [1994], horizontal mixing rates can be calculated self-consistently as the ratio of the E-P flux divergence to the latitudinal gradient of zonal mean potential vorticity, $K_{yy} = -F_{PW}/\bar{q}_y$. This formulation follows from the flux-gradient relationship [e.g., *Newman et al.*, 1988], $\overline{v'q'} = -K_{yy}\bar{q}_y$, where the E-P flux divergence is taken as the zonal mean PV flux for quasi-geostrophic planetary waves.

For the troposphere and stratosphere, we have derived climatological E-P flux divergence and K_{yy} quantities using 17 years (1979-1995) of daily 3-D NCEP analyses for 1000-1 mb. This computation includes the wave dissipation and induced mixing due to both thermal damping and wave breaking. To account for the effects from both planetary and synoptic scale waves in the troposphere and very lower stratosphere, we include zonal wavenumbers 1-12 from the ground to 10 mb. Above this level, zonal waves 1-6 are included since only the planetary scale waves are important in this region.

For the eddy winds in the E-P flux calculations, we used balanced winds computed from daily NCEP geopotential height analyses for regions poleward of $\pm 20°$ [*Randel*, 1992], and HRDI winds for the tropics between $\pm 20°$. Because of data gaps and the limited longitudinal coverage of the daily HRDI data, we used monthly mean HRDI winds and NCEP temperatures for 1992 to 1996 to compute the tropical E-P flux and K_{yy} quantities. Using monthly mean data in this way accounts for the stationary wave components but not the transient eddy contributions. However, the HRDI-based wave

drive and diffusion quantities resulted in model simulated tracer fields in the tropics and subtropics that were in good agreement with observations [*Fleming et al.,* 1999].

For the mesosphere above 1 mbar, F_{PW} and K_{yy} were computed from the CIRA-86 stationary planetary wave climatology [*Barnett and Labitzke*, 1990]. This contains monthly mean temperature and geopotential height data for zonal waves 1-2 based on Nimbus-6 satellite measurements for 1975-1978. As in the stratosphere, balanced winds were used for the eddy winds poleward of $\pm 20°$, with a second derivative balanced wind calculation used in the tropics [*Fleming et al.,* 1990]. Unlike the stratosphere, we did not utilize the HRDI winds in the tropical mesosphere since using different time periods for the eddy temperatures (1975-1978) and eddy winds (1992-1996) was thought to be unsatisfactory for these calculations.

Consistent with previous investigations [*Newman et al.,* 1988], our computations revealed mostly negative areas of E-P flux divergence, but also some positive values, especially at high latitudes. This implies a wave-induced acceleration of the mean flow, and a negative mixing rate via the flux-gradient relationship. While regions of positive F_{PW} may be caused by limitations of the original data sets, some areas of positive E-P flux may be real, and the implied negative K_{yy} indicates a breakdown in the assumptions underlying the flux-gradient relationship. This is also indicative of the ambiguity in interpreting E-P diagnostics for wave propagation and dissipation [e.g., *Andrews*, 1987; *Newman et al.,* 1988].

To avoid computing negative mixing rates in practice, regions of positive E-P flux divergence were set to zero, implying a zero K_{yy}. The resultant F_{PW} fields were smoothed once in the latitude-height domain before being applied in the calculations for $\bar{\chi}^*$ and K_{yy}. To ensure that K_{yy} remains well behaved, we also apply the criterion that $\bar{q}_y \geq 0.5\text{x}10^{-11} m^{-1} s^{-1}$ as suggested by *Randel and Garcia* [1994]. This also avoids negative mixing rates and implies that large positive values of K_{yy} are caused by eddy processes via the E-P flux divergence and not by instability of the zonal mean flow as

represented by small or negative $\bar{q}_y$.

We impose a very small background K_{yy} of $10^8\ cm^2s^{-1}$ throughout the stratosphere and mesosphere. In the low-middle troposphere, we set a large background K_{yy} of $2x10^{10}cm^2s^{-1}$ to simulate the interhemispheric transit time of 1-2 years estimated from SF_6 and halocarbon data near the ground [e.g., *Geller et al.*, 1997]. We also impose a small K_{yy} of $10^8cm^2s^{-1}$ around the tropopause region where the tropopause height changes across adjacent latitudes. This decreased the anomolous cross-tropopause transport and gave better model simulations of water vapor compared with observations in the very lower stratosphere at middle to high latitudes. Because of the uncertainties involved and the relatively small effect, we do not include the transport due to the off-diagonal K_{yz} and K_{zy} terms in the diffusion tensor. These arise from the projection of K_{yy} from isentropes to pressure surfaces [*Newman et al.*, 1988].

Figure A.4 shows the planetary wave driving (F_{PW}) for January. In the troposphere, large wave drive is evident poleward of $\pm 20^o$ during winter and to a lesser extent, summer, due to synoptic and planetary wave activity. These features are similar in both hemispheres (July not shown). Large F_{PW} also occurs in the winter extra-tropical stratosphere and mesosphere.

The corresponding stratospheric K_{yy} fields for January and September are shown in color in Figure A.5, and illustrate the regions of large mixing associated with large planetary wave activity in the winter middle atmosphere. Here we have also overlaid the model CH_4 values to show the effect of strong mixing on the long lived tracer fields, for example as seen in the winter midlatitude surf-zone region in the stratosphere. We note that consistent with *Randel and Garcia* [1994], the direct ratio calculation of K_{yy} gives large mixing rates at high latitudes in the upper stratosphere and lower mesophere, and also at 20°-45°N above 100 mb coincident with weak $\bar{q}_y$ in the surf-zone region. This is in contrast to *Newman et al.* [1988] who computed largest mixing rates only at high latitudes using a linear regression fit of $\overline{v'q'}$ and $\bar{q}_y$ with a zero intercept. Weak mixing

is evident in the tropics and summer hemisphere, except for the very lower summer stratosphere where decaying baroclinic wave activity from the troposphere generates large mixing below 20 km.

The seasonal variation of K_{yy} and $\bar{u}$ at several different levels are shown in Figure A.6. In the mid-upper stratosphere and mesosphere, weak mixing occurs in the easterly flow regimes of the summer hemisphere and in the tropics, consistent with a minimum of planetary wave activity in these regions. Note that the tropical stratospheric mixing rates based on the HRDI winds are weak but not negligible, with values as large as $8\text{x}10^9\ cm^2s^{-1}$. In the mid-late winter, large K_{yy} values are seen along the subtropical edges of the polar night jets, characterizing the surf-zone region of the winter stratosphere. This area of maxima moves poleward during late winter, with large mixing at high latitudes during spring of both hemispheres associated with the deceleration and break up of the polar vorticies. These figures also show the contrasting degree of winter polar vortex isolation in the two hemispheres, reflecting the hemispheric asymmetry in planetary wave activity. Weak mixing occurs in the core of the SH mid-winter vortex, consistent with the inhibition of planetary wave propagation through strong westerly winds [*Charney and Drazin*, 1961]. The NH exhibits significantly weaker $\bar{u}$ and larger K_{yy} throughout the winter stratosphere poleward of 25°N. In the lower mesosphere, both hemispheres show strong subtropical jets near ±35° in mid-winter, with strong mixing occurring mainly on the poleward flanks of the jets. In the very lower stratosphere (68 mb), westerly winds and significant mixing occur throughout much of the year in the extratropics of both hemispheres. There is also evidence of a semi-annual signal in the mixing in both hemispheres, with largest K_{yy} in spring and fall coinciding with the build-up and decrease of the winter polar jets. As at higher levels, weaker mixing at 68 mbar is observed in the tropics, and in mid-winter in the cores of the polar jets, especially in the SH.

A.3.b. Gravity Waves

Computations of vertical eddy diffusion (K_{zz}) and mechanical forcing (F_{GW} in equations A1-A2) from gravity waves are based on the parameterization originally formulated by *Lindzen* [1981] and modified by *Holton and Zhu* [1984] (hereafter HZ84). Other studies have used this parameterization to compute the time evolution of the zonal mean flow [*Schoeberl et al.,* 1983; HZ84; *Garcia and Solomon,* 1985]. However, since $\bar{u}$ and $\bar{T}$ are pre-determined in our model, we compute the seasonal and spatial distribution of wave drag and diffusion based on the empirically determined zonal wind and temperature fields and an input set of gravity wave parameters. These computed wave effects are highly dependent on the background wind field in the middle atmosphere [e.g., *Shine,* 1989]. To account for the longitudinal variations of the background wind which can be significant during the NH winter, we use a 3-D zonal wind field in the parameterization. This wind field is composed of the zonal mean wind described in section A.1, with the longitudinal variability based on NCEP and HRDI data as discussed in section A.3.a. The longitudinal grid resolution is 30° which, although rather coarse, should be sufficient to accomodate the planetary scale features of the middle atmosphere.

In accordance with the tropospheric sources of gravity waves, we assume a spectrum of 9 waves with zonal phase speeds $c = 0, \pm 10, \pm 20, \pm 30, \pm 40\, ms^{-1}$, all with a horizontal wavelength of 200 km (HZ84). Here we have assumed that waves are only traveling zonally, although similar results are obtained by assuming an isotropic spectrum of waves as in HZ84. Following *Garcia et al.* [1992], we include two additional waves in the tropics with phase speeds $c = \pm 50\, ms^{-1}$ and zonal wavelength of 800 km. At the lower boundary (375 mbar), we specify the vertical velocity ($\hat{w_0}$) as a function of the wave phase speed, with the slowest phase velocity waves having the largest $\hat{w_0}$. The velocities range from .03 ms^{-1} for the slowest waves to .002 ms^{-1} for the fastest waves, with these values skewed to have slightly larger values for the westerly waves [*Huang and Smith,*

1991]. We impose only a weak geographical variation on $\hat{w}_0$, with slightly larger values at midlatitudes compared with the tropics and polar regions. To mimic the generation of gravity waves by convection, we also specify slightly larger $\hat{w}_0$ over subtropical land areas during summer following *Wu and Waters* [1996]. However, we note that in our current model formulation, the geographical and seasonal variability in the computed gravity wave effects is determined primarily by the background wind.

For each latitude and longitude, the algorithm determines the breaking level z_{br}, turbulent diffusion, and vertical momentum flux convergence for each wave component. The contributions to diffusion and wave drag are summed over all wave components to obtain distributions of K_{zz} and F_{GW}. We also include in F_{GW} the wave driving due to the turbulent diffusion of zonal momentum. The K_{zz} and F_{GW} values are zonally averaged, and smoothed in latitude and height. Following previous studies, we apply an efficiency factor ($\epsilon = .025$) to K_{zz} and F_{GW} to account for the fact that gravity wave breaking is not continuous, but rather is sporadic in time and space. The values of ϵ and $\hat{w}_0$ (used to determine z_{br}) were specified to compute a wave drag peaking at about 100 $ms^{-1}day^{-1}$ in the upper mesosphere, in rough qualitative agreement with that inferred previously [e.g., *Holton*, 1983; *Fritts and Vincent*, 1987; *Shine*, 1989; *Huang and Smith*, 1991]. Our computed K_{zz} and F_{GW} gave good agreement in the computed seasonal cycle of mesospheric H_2O compared with UARS/HALOE measurements (see Part 1). It may be possible to improve the model simulations by tuning the seasonal and geographical variability of ϵ and $\hat{w}_0$ as observational characterization of gravity waves improve.

We also include a contribution to the zonal mean F_{GW} and K_{zz} from the breaking diurnal tide in the lower thermosphere. In accordance with UARS/HRDI observations [*Lieberman and Hays*, 1994] and theoretical estimates [*Forbes*, 1982], we specify the largest values at the equator at 90-100 km exponentially decreasing in latitude and height, with a semiannual variation maximizing at the equinoxes. Largest values for March at 90 km at the equator are set to -10 $ms^{-1}day^{-1}$ for wave drag and 30 m^2s^{-1}

for diffusion.

The total zonal mean F_{GW} from gravity waves and the diurnal tide is then applied in equations A1-A2. A background K_{zz}, specified to increase from its value at 30 km (section A.3.c) to .3 $m^2 s^{-1}$ in the mesosphere, is added to that due to gravity waves and the diurnal tide. The total K_{zz} is then used in the model transport of chemical constituents. We impose an upper limit of 100 $m^2 s^{-1}$ to accomodate the 2.4 hour time step used for the vertical diffusive transport of constituents.

Figure A.7 shows latitude-height sections of wave drag and vertical diffusion from the gravity wave scheme, diurnal tidal effects, prescribed background, and troposphere/lower stratosphere specification (see section A.3.c). These calculations are consistent with previous model results [e.g., *Garcia and Solomon*, 1985]. The largest wave drag occurs in the middle to upper mesosphere. Values of F_{GW} are opposite in sign to $\bar{u}$ (Figure A.1b) as the gravity wave drag acts to close off the jets in the upper mesosphere, and induce the summer-winter meridional flow pattern (Figure A.1d). The K_{zz} field also shows maxima occurring in regions of large $\bar{u}$ in the mid-latitude upper mesosphere, with a distinct minimum in the tropics. This pattern is very similar to zonally averaged small scale variances seen in UARS microwave limb sounder (MLS) radiance measurements, which may be an indicator of gravity wave activity [*Wu and Waters*, 1996]. The tropopause is also evident in Figure A.7b, as seen by the sharp transition from large K_{zz} in the troposphere to very small values in the stratosphere.

A.3.c. Tropospheric/Stratospheric K_{zz}

In the troposphere and lower stratosphere below 30 km, K_{zz} is based on the climatological temperature lapse rate, and is determined as follows. We specify the largest K_{zz} to be 100 $m^2 s^{-1}$ for the steepest lapse rate observed in the lower troposphere (-8 K/km). Following the analyses of *Mote et al.* [1998] and *Hall and Waugh* [1997], we specify the minimum K_{zz} to be .01 $m^2 s^{-1}$ in the tropical lower stratosphere where the

lapse rate is most stable ($\sim +4K/km$). The K_{zz} values at each grid point throughout the year are then interpolated from these extreme values using the corresponding lapse rate. This methodology assumes that larger mixing occurs in regions of weaker static stability, given that the latter is indicative of stronger convective overturning. Here we have not accounted for the effects induced by instability in the vertical wind shear given the difficulty in quantifying the diffusion due to this process. As seen in Figure A.7b, this K_{zz} profile mimics the large vertical mixing in the troposphere with a sharp decrease in mixing across the tropopause into the lower stratosphere.

A.3.d. Kelvin Waves

Equatorial Kelvin waves are thought to be important in driving the westerly acceleration of the stratospheric SAO and related meridional circulation. To approximate this process, we used the parameterization of *Dunkerton* [1979] and *Gray and Pyle* [1987] along with the empirical $\bar{u}$ and $\bar{T}$ (section A.1) to diagnose the mechanical forcing from thermally damped Kelvin waves (F_{KW} in equations A1-A2). We assume a zonal wave phase speed of 50 ms^{-1} for zonal wavenumber 1. The vertical momentum flux (B) at the bottom boundary (138 mbar) at the equator is specified to be .0105 m^2s^{-2} which is a factor of 1.5 larger than that used by *Gray and Pyle* [1987]. We also used a thermal damping rate (α) which was slightly slower than the 'fast' rates of *Dunkerton* [1979], with a minimum e-folding damping time of 2.7 days near 50 km. We found that specifying these values of B and α resulted in model simulated tracer fields most similar to observations.

Figure A.8 show $\bar{u}$ and the computed F_{KW} quantity at the equator. The zonal mean wind shows the well known SAO signature above 10 mb, with a phase reversal between the upper stratosphere and upper mesosphere. Maximum F_{KW} occurs near the stratopause, with values of 2-3 $ms^{-1}day^{-1}$. There is a semiannual oscillation in F_{KW}, with significant values extending into the upper mesosphere during January

and July, coincident with the weakest westerly $\bar{u}$ in the lower mesosphere. Weakest westerly accelerations in the upper stratosphere and lower mesosphere occur during the equinoxes, when the westerlies are at a maximum. This is consistent with the modeling study of *Dunkerton* [1979] and the observations of *Hirota* [1978].

Finally, we show the total wave driving ($F_{TOT} = F_{PW} + F_{GW} + F_{KW}$) for January in Figure A.9. Gravity wave drag dominates the total throughout the upper mesosphere, with the planetary wave effects being a greater contribution to the total in the stratosphere. The signal in the middle to high latitude troposphere is due to the combination of planetary and baroclinic eddies.

Acknowledgments. We thank the NASA Atmospheric Chemistry Modeling and Analysis Program and the UARS Science Investigation Program for support of this project.

References

Andrews, D.G., On the interpretation of the Eliassen-Palm flux divergence, *Q.J.R. Meteorol. Soc., 113*, 323-338, 1987.

Andrews, D.G., J.R. Holton, and C.B. Leovy, *Middle Atmosphere Dynamics*, 498 pp., Academic, San Diego, Calif., 1987.

Andrews, A.E., K.A. Boering, B.C. Daube, S.C. Wofsy, E.J. Hintsa, E.M. Weinstock, and T.P. Bui, Empirical age spectra for the lower tropical stratosphere from in situ observations of CO_2: Implications for stratospheric transport, *J. Geophys. Res.*, in press, 1999.

Bacmeister, J.T, M.R. Schoeberl, M.E. Summers, J. Rosenfield, and X. Zhu, Descent of long lived trace gases in the winter polar vortex, *J. Geophys. Res., 100*, 11669-11684, 1995.

Bacmeister, J.T, D.E. Siskind, M.E. Summers, S.D. Eckermann, Age of air in a zonally averaged two-dimensional model, *J. Geophys. Res., 103*, 11263-11288, 1998.

Barnett, J.J., and K. Labitzke, Climatological distribution of planetary waves in the middle atmosphere, *COSPAR International Reference Atmosphere: 1986, Part II: Middle Atmosphere Models, Adv. Space Res., 10, No. 12*, 63-91, 1990.

Boering, K.A., S.C. Wofsy, B.C. Daube, H.R. Schneider, M. Loewenstein, J.R. Podolske, and T.J. Conway, Stratospheric mean ages and transport rates from observations of carbon dioxide and nitrous oxide, *Science, 274*, 1340-1343, 1996.

Brasseur, G., M.H. Hitchman, S. Walters, M. Dymek, E. Falise, and M. Pirre, An interactive chemical dynamical radiative two-dimensional model of the middle atmosphere, *J. Geophys. Res., 95*, 5639-5655, 1990.

Chandra, S., C.H. Jackman, E.L. Fleming, and J.M. Russell III, The seasonal and long term changes in mesospheric water vapor, *Geophys. Res. Lett., 24*, 639-642, 1997.

Charney, J.G., and P.G. Drazin, Propagation of planetary scale disturbances from the lower into the upper atmosphere, *J. Geophys. Res., 66*, 83-109, 1961.

Choi, W.K., and J.R. Holton, Transport of N2O in the stratosphere related to the equatorial semiannual oscillation, *J. Geophys. Res., 96*, 22543-22557, 1991.

DeMore, W.B., S.P. Sander, D.M. Golden, R.F. Hampson, M.J. Kurylo, C.J. Howard, A.R.

Ravishankara, C.E. Kolb, and M.J. Molina, Chemical kinetics and photochemical data for use in stratospheric modeling, Evaluation number 12, *JPL Publ., 97-4*, 266 pp., 1997.

Douglass, A.R., C.H. Jackman, R.S. Stolarski, Comparison of model results transporting the odd nitrogen family with results transporting separate odd nitrogen species, *J. Geophys. Res., 94*, 9862-9872, 1989.

Dunkerton, T.J., On the mean meridional mass motions of the stratosphere and mesosphere, *J. Atmos. Sci., 35*, 2325-2333, 1978.

Dunkerton, T.J., On the role of the Kelvin wave in the westerly phase of the semi-annual zonal wind oscillation, *J. Atmos. Sci., 36*, 32-41, 1979.

Elkins, J.W., *et al.*, Airborne gas chromatograph for in situ measurements of long-lived species in the upper troposphere and lower stratosphere, *Geophys. Res. Lett., 23*, 347-350, 1996.

Eluszkiewicz, J., et al., Residual circulation in the stratosphere and lower mesosphere as diagnised from microwave limb sounder data, *J. Atmos. Sci., 53*, 217-240, 1996.

Fleming, E.L., S. Chandra, J.J. Barnett, and M. Corney, Zonal mean temperature, pressure, zonal wind, and geopotential height as functions of latitude, *COSPAR International Reference Atmosphere: 1986, Part II: Middle Atmosphere Models, Adv. Space Res., 10, No. 12*, 11-59, 1990.

Fleming, E.L., C.H. Jackman, R.S. Stolarski, and D.B. Considine, Simulation of stratospheric tracers using an improved empirically-based two-dimensional model transport formulation, *J. Geophys. Res.*, (in press), 1999.

Forbes, J.M., Atmospheric tides 1. Model description and results for the solar diurnal component, *J. Geophys. Res., 87*, 5222-5240, 1982.

Fritts, D.C., and and R.A. Vincent, Mesospheric momentum flux studies at Adelaide, Australia: Observations and a gravity wave-tidal interaction model, *J. Atmos. Sci., 44*, 605-619, 1987.

Garcia, R.R., Parameterization of planetary wave breaking in the middle atmosphere, *J. Atmos. Sci., 48*, 1405-1419, 1991.

Garcia, R.R., and S. Solomon, The effect of breaking gravity waves on the dynamics and chemical composition of the mesosphere and lower thermosphere, *J. Geophys. Res., 90*, 3850-3868, 1985.

Garcia, R.R., F. Stordal, S. Solomon, and J.T. Kiehl, A new numerical model of the middle atmosphere, 1. Dynamics and transport of tropospheric source gases, *J. Geophys. Res., 97*, 12967-12991, 1992.

Geller, L.S., J.W. Elkins, J.M. Lobert, A.D. Clarke, D.F. Hurst, J.H. Butler, and R.C. Myers, Tropospheric SF_6: Observed latitudinal distribution and trends, derived emissions and interhemispheric exchange time, *Geophys. Res. Lett., 24*, 675-678, 1997.

Gray, L.J., and J.A. Pyle, Two-dimensional model studies of equatorial dynamics and tracer distributions, *Q.J.R. Meteorol. Soc., 113*, 635-651, 1987.

Hall, T.M., and R.A. Plumb, Age as a diagnostic of stratospheric transport, *J. Geophys. Res., 99*, 1059-1070, 1994.

Hall, T.M., and D.W. Waugh, Tracer transport in the tropical stratosphere due to vertical diffusion and horizontal mixing, *Geophys. Res. Lett., 24*, 1383-1386, 1997.

Hall, T.M., and D.W. Waugh, Influence of nonlocal chemistry on tracer distributions: Inferring the mean age of air from SF_6, *J. Geophys. Res., 103*, 13327-13336, 1998.

Hall, T.M., D.W. Waugh, K.A. Boering, and R.A. Plumb, Evaluation of transport in stratospheric models, *J. Geophys. Res., 104*, 18815-18839, 1999.

Harnisch, J., R. Borchers, P. Fabian, and M. Maiss, Tropospheric trends for CF_4 and C_2F_6 since 1982 derived from SF_6 dated stratospheric air *Geophys. Res. Lett., 23*, 1099-1102, 1996.

Haynes, P.H., C.J. Marks, M.E. McIntyre, T.G. Shepherd, and K.P. Shine, On the 'downward control' of extratropical diabatic circulations by eddy-induced mean zonal forces, *J. Atmos. Sci., 48*, 651-678, 1991.

Hirota, I., Equatorial waves in the upper stratosphere and mesosphere in relation to the semiannual oscillation of the zonal wind, *J. Atmos. Sci., 35*, 714-722, 1978.

Holton, J.R., The influence of gravity wave breaking on the general circulation of the middle atmosphere, *J. Atmos. Sci., 40*, 2497-2507, 1983.

Holton, J.R., and X. Zhu, A further study of gravity wave induced drag and diffusion in the mesosphere, *J. Atmos. Sci., 41*, 2653-2662, 1984.

Holton, J.R., and M.R. Schoeberl, The role of gravity wave generated advection and diffusion in transport of tracers in the mesosphere *J. Geophys. Res., 93*, 11075-11082, 1988.

Huang, T.Y.W., and A.K. Smith, The mesospheric diabatic circulation and the parameterized thermal effect of gravity wave breaking on the circulation, *J. Atmos. Sci., 48*, 1093-1111, 1991.

Inter-governmental Panel on Climate Change (IPCC), *Special Report on Aviation and the Global Atmosphere*, 1999.

Jackman, C.H., A.R. Douglass, R.B. Rood, R.D. McPeters, and P.E. Meade, Effect of solar proton events on the middle atmosphere during the past two solar cycles as computed using a two-dimesional model, *J. Geophys. Res., 95*, 7417-7428, 1990.

Jackman, C.H., A.R. Douglass, K.F. Brueske, and S.A. Klein, The influence of dynamics on two-dimensional model results: Simulations of ^{14}C and stratospheric NO_x injections, *J. Geophys. Res., 96*, 22559-22572, 1991.

Jackman, C.H., E.L. Fleming, S. Chandra, D.B. Considine, and J.E. Rosenfield, Past, present, and future modeled ozone trends with comparisons to observed trends, *J. Geophys. Res., 101*, 28753-28767, 1996.

Kalnay E., *et al.,* The NCEP/NCAR 40-year reanalysis project, *Bull. Amer. Meteor. Soc., 77*, 437-471, 1996.

Kawa, S. R. et al., Editors, Assessment of the Effects of High Speed Aircraft in the Stratosphere: 1998, *NASA Reference Publication NASA/TM-1999-209237*, 1999.

Kinnison, D. E., H. S. Johnston, H. S., and D.J. Wuebbles, Model study of atmospheric transport using carbon 14 and strontium 90 data as inert tracers, *J. Geophys. Res., 99*, 20647-20664, 1994.

Ko, M.K.W., H.R. Schneider, R.L. Shia, D.K. Weisenstein, and N.D. Sze, A two- dimensional model with coupled dynamics, radiation, and photochemistry, 1. Simulation of the middle atmosphere, *J. Geophys. Res., 98*, 20429-20440, 1993.

Lieberman, R.S., and P.B. Hays, An estimate of the momentum deposition in the lower

thermosphere by the observed diurnal tide, *J. Atmos. Sci., 51*, 3094-3105, 1994.

Lindzen, R. S., Turbulence and stress owing to gravity wave and tidal breakdown, *J. Geophys. Res., 86*, 9707-9714, 1981.

Lindzen, R. S., and H.L. Kuo, A reliable method for the numerical integration of a large class of ordinary and partial differential equations, *Mon. Weather Rev., 96*, 732-734, 1969.

McPeters, R.D., D.F. Heath, and P.K. Bhartia, Average ozone profiles for 1979 from the Nimbus-7 SBUV instrument, *J. Geophys. Res., 89*, 5199-5214, 1984.

Moore, F.L., J.W. Elkins, E.A. Ray, G.S. Dutton, R.E. Dunn, D.W. Fahey, R.J. McLaughlin, and T.L. Thompson, First in situ gas chromatograph on a balloon platform yielding tracer measurements with improved spatial resolution, (manuscript in preparation), 1999.

Mote, P.W., T.J. Dunkerton, M.E. McIntyre, E.A. Ray, P.H. Haynes, and J.M. Russell III, Vertical velocity, vertical diffusion, and dilution by midlatitude air in the tropical lower stratosphere, *J. Geophys. Res., 103*, 8651-8666, 1998.

Nedoluha, G.E., R.M. Bevilacqua, R.M. Gomez, W.B. Waltman, B.C. Hicks, D.L. Thacker, and W.A. Matthews, Measurements of water vapor in the middle atmosphere and implication for mesospheric transport, *J. Geophys. Res., 101*, 21183-21193, 1996.

Newell, R.E., J.W. Kidson, D.G. Vincent, and G.J. Boer, *The General Circulations of the Tropical Atmosphere*, vol. 2, chapter 7, MIT Press, Cambridge, Mass., 1974.

Newman, P.A., M.R. Schoeberl, R.A. Plumb, and J.E. Rosenfield, Mixing rates calculated from potential vorticity, *J. Geophys. Res., 93*, 5221-5240, 1988.

Newman, P.A., and J.E. Rosenfield, Stratospheric thermal damping times, *Geophys. Res. Lett., 24*, 433-436, 1997.

Nightingale, R.W., et al., Global CF_2Cl_2 measurements by UARS cryogenic limb array etalon spectrometer: Validation by correlative data and a model, *J. Geophys. Res., 101*, 9711-9736, 1996.

Oort, A.H., *Global Atmospheric Circulation Statistics, 1958-1983*, NOAA Profesional Paper 14, 1983.

Park, J. H., M. K. W. Ko, C. H. Jackman, and R. A. Plumb, Editors, Report of the 1997

Models and Measurements Workshop, held November 3-5, 1997, Williamsburg, Virginia, *NASA Reference Publication XXXX*, 1999.

Plumb, R.A., A "tropical pipe" model of stratospheric transport, *J. Geophys. Res., 101*, 3957-3972, 1996.

Randel, W.J., Global atmospheric circulation statistics, 1000-1 mb, NCAR Tech. Note, TN-36STR, 256 pp., 1992.

Randel, W.J., and R.R. Garcia, Application of a planetary wave breaking parameterization to stratospheric circulation statistics, *J. Atmos. Sci., 51*, 1157-1168, 1994.

Ray, E.A., F.L. Moore, J.W. Elkins, G.S. Dutton, D.W. Fahey, H. Vomel, S.J. Oltmans, and K.H. Rosenlof, Transport into the Northern Hemisphere lowermost stratosphere revealed by in situ tracer measurements, *J. Geophys. Res.*, in press, 1999.

Remsberg, E.E., J.M. Russell III, and C.Y. Wu, An interim reference model for the variability of the middle atmosphere H_2O vapor distribution, *Handbook for Middle Atmosphere Program, 31*, 50-66, 1989.

Rosenfield, J.E., P.A. Newman, and M.R. Schoeberl, Computations of diabatic descent in the stratospheric polar vortex, *J. Geophys. Res., 99*, 16677-16689, 1994.

Rosenlof, K.H., and J.R. Holton, Estimates of the stratospheric residual circulation using the downward control principle, *J. Geophys. Res., 98*, 10465-10479, 1993.

Schoeberl, M.R., D.F. Strobel, and J.P. Apruzese, A numerical model of gravity wave breaking and stress in the mesosphere, *J. Geophys. Res., 88*, 5249-5259, 1983.

Shine, K., Sources and sinks of zonal momentum in the middle atmosphere daignosed using the diabatic circulation, *Q.J.R. Meteorol. Soc., 115*, 265-292, 1989.

Smith, A.K., and G.P. Brasseur, Numerical simulation of the seasonal variation of mesospheric water vapor, *J. Geophys. Res., 96*, 7553-7563, 1991.

Stolarski, R.S., et al., Scientific assessment of the atmospheric effects of stratospheric aircraft, *NASA Ref. Pub., 1381*, 110 pp., 1995.

Strahan, S.E., A.R. Douglass, J.E. Nielsen, and K.A. Boering, The CO_2 seasonal cycle as a tracer of transport, *J. Geophys. Res., 103*, 13729-13741, 1998.

Volk, C.M., *et al.*, Evaluation of source gas lifetimes from stratospheric observations, *J.*

Geophys. Res., 102, 25543-25564, 1997.

Waugh, D.W., *et al.*, Three-dimensional simulations of long-lived tracers using winds from MACCM2, *J. Geophys. Res., 102*, 21493-21513, 1997.

World Meteorological Organization (WMO), Scientific Assessment of Ozone Depletion: 1994, *Rep. 37* Global Ozone Research and Monitoring Project, Geneva, 1995.

World Meteorological Organization (WMO), Scientific Assessment of Ozone Depletion: 1998, *Rep. 44* Global Ozone Research and Monitoring Project, Geneva, 1999.

Wu, D.L., and J.W. Waters, Satellite observations of atmospheric variances: A possible indication of gravity waves, *Geophys. Res. Lett., 23*, 3631-3634, 1996.

Yang, H., E. Olaguer, and K.-K. Tung, Simulation of the present-day atmospheric ozone, odd nitrogen, chlorine, and other species using a coupled 2-D model in isentropic coordinates *J. Atmos. Sci., 48*, 442-471, 1991.

This manuscript was prepared with the AGU LaTeX macros v3.0.

Figure Captions

Figure 1. Vertical profiles of carbon 14 at 31°N for July 1964 and July 1966. Plotted are the time dependent model simulations for base scenario A (solid line) and the four circulation scenarios B-E listed in Table 1: very weak circulation (B, dashed-triple dot line); weak circulation (C, dashed line); strong circulation (D, dashed-dot line); and very strong circulation (E, dotted line). Also shown are the observations from *Kinnison et al.* [1994] (dashed-asterisk line). Values are in mixing ratio units, defined as 10^5 atoms of ^{14}C per gram of dry air.

Figure 1. Vertical profiles of carbon 14 at 31°N for July 1964 and July 1966. Plotted are the time dependent model simulations for base scenario A (solid line) and the four circulation scenarios B-E listed in Table 1: very weak circulation (B, dashed-triple dot line); weak circulation (C, dashed line); strong circulation (D, dashed-dot line); and very strong circulation (E, dotted line). Also shown are the observations from *Kinnison et al.* [1994] (dashed-asterisk line). Values are in mixing ratio units, defined as 10^5 atoms of ^{14}C per gram of dry air.

Figure 2. Annually averaged mean age of air (years) derived from time dependent model simulations of SF_6 for the base scenario A and the four circulation scenarios B-E listed in Table 1. The age is taken relative to the global mean value at the surface. The contour interval is 1 year.

Figure 2. Annually averaged mean age of air (years) derived from time dependent model simulations of SF_6 for the base scenario A and the four circulation scenarios B-E listed in Table 1. The age is taken relative to the global mean value at the surface. The contour interval is 1 year.

Figure 3. Age of air derived from SF_6 as a function of latitude for October/November 1994 using ER-2 measurements at 19-21 km (triangles) and the model circulation scenarios listed in Table 1 at 20 km (lines). Included are the base model scenario (A, solid line), the very weak circulation (B, dashed-triple dot line), the weak circulation (C, dashed line), the strong circulation (D, dashed-dot line), and the very strong circulation (E, dotted line). The age is taken relative to the global mean value at the surface.

Figure 3. Age of air derived from SF_6 as a function of latitude for October/November 1994 using ER-2 measurements at 19-21 km (triangles) and the model circulation scenarios listed in Table 1 at 20 km (lines). Included are the base model scenario (A, solid line), the very weak circulation (B, dashed-triple dot line), the weak circulation (C, dashed line), the strong circulation (D, dashed-dot line), and the very strong circulation (E, dotted line). The age is taken relative to the global mean value at the surface.

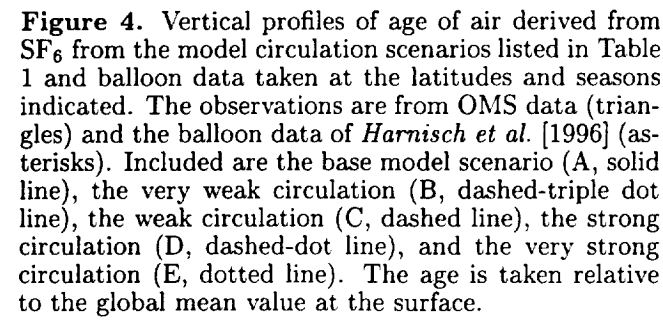

Figure 4. Vertical profiles of age of air derived from SF_6 from the model circulation scenarios listed in Table 1 and balloon data taken at the latitudes and seasons indicated. The observations are from OMS data (triangles) and the balloon data of *Harnisch et al.* [1996] (asterisks). Included are the base model scenario (A, solid line), the very weak circulation (B, dashed-triple dot line), the weak circulation (C, dashed line), the strong circulation (D, dashed-dot line), and the very strong circulation (E, dotted line). The age is taken relative to the global mean value at the surface.

Figure 4. Vertical profiles of age of air derived from SF_6 from the model circulation scenarios listed in Table 1 and balloon data taken at the latitudes and seasons indicated. The observations are from OMS data (triangles) and the balloon data of *Harnisch et al.* [1996] (asterisks). Included are the base model scenario (A, solid line), the very weak circulation (B, dashed-triple dot line), the weak circulation (C, dashed line), the strong circulation (D, dashed-dot line), and the very strong circulation (E, dotted line). The age is taken relative to the global mean value at the surface.

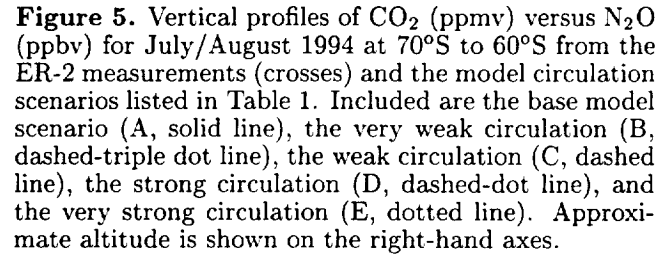

Figure 5. Vertical profiles of CO_2 (ppmv) versus N_2O (ppbv) for July/August 1994 at 70°S to 60°S from the ER-2 measurements (crosses) and the model circulation scenarios listed in Table 1. Included are the base model scenario (A, solid line), the very weak circulation (B, dashed-triple dot line), the weak circulation (C, dashed line), the strong circulation (D, dashed-dot line), and the very strong circulation (E, dotted line). Approximate altitude is shown on the right-hand axes.

Figure 5. Vertical profiles of CO_2 (ppmv) versus N_2O (ppbv) for July/August 1994 at 70°S to 60°S from the ER-2 measurements (crosses) and the model circulation scenarios listed in Table 1. Included are the base model scenario (A, solid line), the very weak circulation (B, dashed-triple dot line), the weak circulation (C, dashed line), the strong circulation (D, dashed-dot line), and the very strong circulation (E, dotted line). Approximate altitude is shown on the right-hand axes.

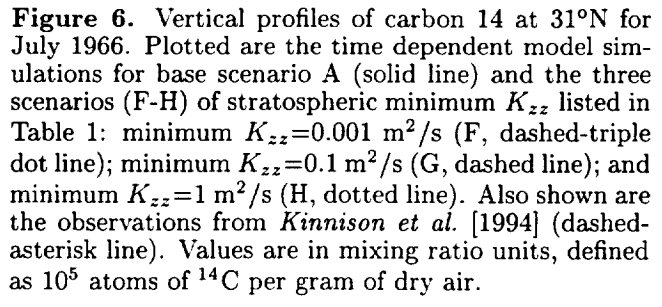

Figure 6. Vertical profiles of carbon 14 at 31°N for July 1966. Plotted are the time dependent model simulations for base scenario A (solid line) and the three scenarios (F-H) of stratospheric minimum K_{zz} listed in Table 1: minimum K_{zz}=0.001 m^2/s (F, dashed-triple dot line); minimum K_{zz}=0.1 m^2/s (G, dashed line); and minimum K_{zz}=1 m^2/s (H, dotted line). Also shown are the observations from *Kinnison et al.* [1994] (dashed-asterisk line). Values are in mixing ratio units, defined as 10^5 atoms of ^{14}C per gram of dry air.

Figure 6. Vertical profiles of carbon 14 at 31°N for July 1966. Plotted are the time dependent model simulations for base scenario A (solid line) and the three scenarios (F-H) of stratospheric minimum K_{zz} listed in Table 1: minimum K_{zz}=0.001 m^2/s (F, dashed-triple dot line); minimum K_{zz}=0.1 m^2/s (G, dashed line); and minimum K_{zz}=1 m^2/s (H, dotted line). Also shown are the observations from *Kinnison et al.* [1994] (dashed-asterisk line). Values are in mixing ratio units, defined as 10^5 atoms of ^{14}C per gram of dry air.

Figure 7. Annually averaged mean age of air (years) derived from time dependent model simulations of SF_6 for the base scenario A and the three scenarios (F-H) of stratospheric minimum K_{zz} listed in Table 1. The age is taken relative to the global mean value at the surface. The contour interval is 1 year.

Figure 7. Annually averaged mean age of air (years) derived from time dependent model simulations of SF_6 for the base scenario A and the three scenarios (F-H) of stratospheric minimum K_{zz} listed in Table 1. The age is taken relative to the global mean value at the surface. The contour interval is 1 year.

Figure 8. Age of air derived from SF_6 as a function of latitude for October/November 1994 using ER-2 measurements at 19-21 km (triangles) and the model scenarios of stratospheric minimum K_{zz} listed in Table 1 at 20 km (lines). Included are the base model scenario (A, solid line), minimum K_{zz}=0.001 m^2/s (F, dashed-triple dot line); minimum K_{zz}=0.1 m^2/s (G, dashed line); and minimum K_{zz}=1 m^2/s (H, dotted line). The age is taken relative to the global mean value at the surface.

Figure 8. Age of air derived from SF_6 as a function of latitude for October/November 1994 using ER-2 measurements at 19-21 km (triangles) and the model scenarios of stratospheric minimum K_{zz} listed in Table 1 at 20 km (lines). Included are the base model scenario (A, solid line), minimum K_{zz}=0.001 m^2/s (F, dashed-triple dot line); minimum K_{zz}=0.1 m^2/s (G, dashed line); and minimum K_{zz}=1 m^2/s (H, dotted line). The age is taken relative to the global mean value at the surface.

Figure 9. Vertical profiles of age of air derived from SF_6 from the model scenarios of stratospheric minimum K_{zz} listed in Table 1 and balloon data taken during September near 40°N. The observations are from OMS data (triangles) and the balloon data of *Harnisch et al.* [1996] (asterisks). Included are the base model scenario (A, solid line), the minimum K_{zz}=0.001 m^2/s (F, dashed-triple dot line); minimum K_{zz}=0.1 m^2/s (G, dashed line); and minimum K_{zz}=1 m^2/s (H, dotted line). The age is taken relative to the global mean value at the surface.

Figure 9. Vertical profiles of age of air derived from SF_6 from the model scenarios of stratospheric minimum K_{zz} listed in Table 1 and balloon data taken during September near 40°N. The observations are from OMS data (triangles) and the balloon data of *Harnisch et al.* [1996] (asterisks). Included are the base model scenario (A, solid line), the minimum K_{zz}=0.001 m^2/s (F, dashed-triple dot line); minimum K_{zz}=0.1 m^2/s (G, dashed line); and minimum K_{zz}=1 m^2/s (H, dotted line). The age is taken relative to the global mean value at the surface.

Figure 10. Seasonal profiles of zonal and monthly mean H_2O from the HALOE version 19 data (dashed-asterisk) and three model scenarios at 80 km (.01 mbar) for 45°N, equator, and 45°S. Included are the base scenario (A, solid line), and scenarios with weak (I, dashed line) and strong (J, dotted line) mesospheric gravity wave effects.

Figure 10. Seasonal profiles of zonal and monthly mean H_2O from the HALOE version 19 data (dashed-asterisk) and three model scenarios at 80 km (.01 mbar) for 45°N, equator, and 45°S. Included are the base scenario (A, solid line), and scenarios with weak (I, dashed line) and strong (J, dotted line) mesospheric gravity wave effects.

Figure 11. Annually averaged mean age of air (years) derived from time dependent model simulations of SF_6 for the base scenario A and the 7 K_{yy} scenarios (K-Q) listed in Table 1. In panels a-d and g-h, the K_{yy} and wave drive are changed above the tropopause. Scenario (Q) in panel f is the same as the base case (scenario A, panel e), except K_{yy} has been set to a very small constant value of $10^8 cm^2/s$ throughout the tropical stratosphere (15°S-15°N, 15-50 km) for all seasons. In all panels, the age is taken relative to the global mean value at the surface. The contour interval is 1 year.

Figure 11. Annually averaged mean age of air (years) derived from time dependent model simulations of SF_6 for the base scenario A and the 7 K_{yy} scenarios (K-Q) listed in Table 1. In panels a-d and g-h, the K_{yy} and wave drive are changed above the tropopause. Scenario (Q) in panel f is the same as the base case (scenario A, panel e), except K_{yy} has been set to a very small constant value of $10^8 cm^2/s$ throughout the tropical stratosphere (15°S-15°N, 15-50 km) for all seasons. In all panels, the age is taken relative to the global mean value at the surface. The contour interval is 1 year.

Figure 12. Age of air derived from SF_6 as a function of latitude for October/November 1994 using ER-2 measurements at 19-21 km (triangles) and several model K_{yy} scenarios listed in Table 1 at 20 km (lines). Included are the base model scenario (A, solid line), K_{yy} reduced by a factor of 5 above the tropopause (K, dashed-triple dot line), K_{yy} reduced by a factor of 2 above the tropopause (L, dashed line), K_{yy} increased by a factor of 2 above the tropopause (M, dashed-dot line), K_{yy} increased by a factor of 5 above the tropopause (N, dotted line), and the base model with K_{yy} set to a very small constant value of $10^8 cm^2/s$ throughout the tropical stratosphere (15°S-15°N, 15-50 km) for all seasons (Q, sold-asterisk line). The age is taken relative to the global mean value at the surface.

Figure 12. Age of air derived from SF_6 as a function of latitude for October/November 1994 using ER-2 measurements at 19-21 km (triangles) and several model K_{yy} scenarios listed in Table 1 at 20 km (lines). Included are the base model scenario (A, solid line), K_{yy} reduced by a factor of 5 above the tropopause (K, dashed-triple dot line), K_{yy} reduced by a factor of 2 above the tropopause (L, dashed line), K_{yy} increased by a factor of 2 above the tropopause (M, dashed-dot line), K_{yy} increased by a factor of 5 above the tropopause (N, dotted line), and the base model with K_{yy} set to a very small constant value of $10^8 cm^2/s$ throughout the tropical stratosphere (15°S-15°N, 15-50 km) for all seasons (Q, sold-asterisk line). The age is taken relative to the global mean value at the surface.

Figure 13. Vertical profiles of age of air derived from SF_6 from several model K_{yy} scenarios listed in Table 1, and balloon data taken at the latitudes and seasons indicated. The observations are from OMS data (triangles) and the balloon data of *Harnisch et al.* [1996] (asterisks). Included are the base model scenario (A, solid line), K_{yy} reduced by a factor of 5 above the tropopause (K, dashed-triple dot line), K_{yy} reduced by a factor of 2 above the tropopause (L, dashed line), K_{yy} increased by a factor of 2 above the tropopause (M, dashed-dot line), and K_{yy} increased by a factor of 5 above the tropopause (N, dotted line). The age is taken relative to the global mean value at the surface.

Figure 13. Vertical profiles of age of air derived from SF_6 from several model K_{yy} scenarios listed in Table 1, and balloon data taken at the latitudes and seasons indicated. The observations are from OMS data (triangles) and the balloon data of *Harnisch et al.* [1996] (asterisks). Included are the base model scenario (A, solid line), K_{yy} reduced by a factor of 5 above the tropopause (K, dashed-triple dot line), K_{yy} reduced by a factor of 2 above the tropopause (L, dashed line), K_{yy} increased by a factor of 2 above the tropopause (M, dashed-dot line), and K_{yy} increased by a factor of 5 above the tropopause (N, dotted line). The age is taken relative to the global mean value at the surface.

Figure 14. Age of air derived from SF_6 as a function of latitude for October/November 1994 using ER-2 measurements at 19-21 km (triangles) and several model K_{yy} scenarios listed in Table 1 at 20 km (lines). Included are the base model scenario (A, solid line), and the scenarios with K_{yy} reduced by a factor of 5 above the tropopause (K, dashed-triple dot line) and K_{yy} increased by a factor of 5 above the tropopause (N, dotted line) as in Figure 12. Also included are scenarios in which both the K_{yy} and wave drive have been reduced by a factor of 5 above the tropopause (O, dashed-dot line), and increased by a factor of 5 above the tropopause (P, dashed line). The age is taken relative to the global mean value at the surface.

Figure 14. Age of air derived from SF_6 as a function of latitude for October/November 1994 using ER-2 measurements at 19-21 km (triangles) and several model K_{yy} scenarios listed in Table 1 at 20 km (lines). Included are the base model scenario (A, solid line), and the scenarios with K_{yy} reduced by a factor of 5 above the tropopause (K, dashed-triple dot line) and K_{yy} increased by a factor of 5 above the tropopause (N, dotted line) as in Figure 12. Also included are scenarios in which both the K_{yy} and wave drive have been reduced by a factor of 5 above the tropopause (O, dashed-dot line), and increased by a factor of 5 above the tropopause (P, dashed line). The age is taken relative to the global mean value at the surface.

Figure 15. Annually averaged mean age of air (years) derived from time dependent model simulations of SF_6. Included are the base scenario A and the four combination transport scenarios (S-V) listed in Table 1. Also included is the simulation from the previous 1995 version of the model transport in panel f (scenario W). In all panels, the age is taken relative to the global mean value at the surface. The contour interval is 1 year.

Figure 15. Annually averaged mean age of air (years) derived from time dependent model simulations of SF_6. Included are the base scenario A and the four combination transport scenarios (S-V) listed in Table 1. Also included is the simulation from the previous 1995 version of the model transport in panel f (scenario W). In all panels, the age is taken relative to the global mean value at the surface. The contour interval is 1 year.

Figure 16. Age of air derived from SF_6 as a function of latitude for October/November 1994 using ER-2 measurements at 19-21 km (triangles) and several model scenarios listed in Table 1 at 20 km (lines). Included are the base model scenario (A, solid line), scenario S (dashed-triple dot line) which combines scenarios C, F, and M to give a moderately long stratospheric residence time, scenario T (dotted line) which combines scenarios D, G, and L to give a moderately short stratospheric residence time, and scenario W (dashed line) which uses the previous 1995 version of the model transport. The age is taken relative to the global mean value at the surface.

Figure 16. Age of air derived from SF_6 as a function of latitude for October/November 1994 using ER-2 measurements at 19-21 km (triangles) and several model scenarios listed in Table 1 at 20 km (lines). Included are the base model scenario (A, solid line), scenario S (dashed-triple dot line) which combines scenarios C, F, and M to give a moderately long stratospheric residence time, scenario T (dotted line) which combines scenarios D, G, and L to give a moderately short stratospheric residence time, and scenario W (dashed line) which uses the previous 1995 version of the model transport. The age is taken relative to the global mean value at the surface.

Figure 17. Vertical profiles of age of air derived from SF_6 from several model scenarios listed in Table 1, and balloon data taken at the latitudes and seasons indicated. The observations are from OMS data (triangles) and the balloon data of *Harnisch et al.* [1996] (asterisks). Included are the base model scenario (A, solid line), scenario S (dashed-triple dot line) which combines scenarios C, F, and M to give a moderately long stratospheric residence time, scenario T (dotted line) which combines scenarios D, G, and L to give a moderately short stratospheric residence time, and scenario W (dashed line) which uses the previous 1995 version of the model transport. The age is taken relative to the global mean value at the surface.

Figure 17. Vertical profiles of age of air derived from SF_6 from several model scenarios listed in Table 1, and balloon data taken at the latitudes and seasons indicated. The observations are from OMS data (triangles) and the balloon data of *Harnisch et al.* [1996] (asterisks). Included are the base model scenario (A, solid line), scenario S (dashed-triple dot line) which combines scenarios C, F, and M to give a moderately long stratospheric residence time, scenario T (dotted line) which combines scenarios D, G, and L to give a moderately short stratospheric residence time, and scenario W (dashed line) which uses the previous 1995 version of the model transport. The age is taken relative to the global mean value at the surface.

Figure 18. Scatter plots of the annual and globally averaged mixing ratio (ppbv) of Cl_y (top) and N_2O (bottom), versus mean age (years) at 27 km for the 23 transport scenarios as listed in Table 1. Letters for each scenario are color coded according to the type of transport variation imposed, as indicated in the legend.

Figure 18. Scatter plots of the annual and globally averaged mixing ratio (ppbv) of Cl_y (top) and N_2O (bottom), versus mean age (years) at 27 km for the 23 transport scenarios as listed in Table 1. Letters for each scenario are color coded according to the type of transport variation imposed, as indicated in the legend.

Figure 19. Scatter plots of the annual, global, and stratospherically averaged (pressure weighted) lifetime (years) of $CFCl_3$ (top) and N_2O (bottom), versus mean age (years) for the 23 transport scenarios listed in Table 1. Letters for each scenario are color coded according to the type of transport variation imposed, as indicated in the legend. Also included are the best empirical lifetime estimates (solid line) and the correspoding 1 standard deviation uncertainties (dashed lines) from *Volk et al.* [1997].

Figure 19. Scatter plots of the annual, global, and stratospherically averaged (pressure weighted) lifetime (years) of $CFCl_3$ (top) and N_2O (bottom), versus mean age (years) for the 23 transport scenarios listed in Table 1. Letters for each scenario are color coded according to the type of transport variation imposed, as indicated in the legend. Also included are the best empirical lifetime estimates (solid line) and the correspoding 1 standard deviation uncertainties (dashed lines) from *Volk et al.* [1997].

Figure A.1. Latitude-height sections of zonal mean temperature, zonal wind, and residual vertical velocity and horizontal velocity from the model transport. The contour intervals are 10 K for temperature; 10 m/s for zonal wind; 0.5 cm/s for $\bar{w}^*$ including the contours for $\pm.2, \pm.1$, and $\pm.05$ cm/s; and 2 m/s for $\bar{v}^*$ including the contours for $\pm1, \pm.5$, and $\pm.2$ m/s. Negative values are shaded.

Figure A.1. Latitude-height sections of zonal mean temperature, zonal wind, and residual vertical velocity and horizontal velocity from the model transport. The contour intervals are 10 K for temperature; 10 m/s for zonal wind; 0.5 cm/s for $\bar{w}^*$ including the contours for $\pm.2, \pm.1$, and $\pm.05$ cm/s; and 2 m/s for $\bar{v}^*$ including the contours for $\pm1, \pm.5$, and $\pm.2$ m/s. Negative values are shaded.

Figure A.2. Model simulation of CH_4 in ppbv (color) for January and September, along with streamlines depicting the sense of the model residual circulation $(\bar{v}^*, \bar{w}^*)$. $\bar{w}^*$ has been multiplied by a deformation factor of 200, approximating the ratio of N/f.

Figure A.2. Model simulation of CH_4 in ppbv (color) for January and September, along with streamlines depicting the sense of the model residual circulation $(\bar{v}^*, \bar{w}^*)$. $\bar{w}^*$ has been multiplied by a deformation factor of 200, approximating the ratio of N/f.

Figure A.3. Latent heating rates (a), net diabatic heating (b), net gravity wave heating (c), and the total heating rate (d) for January. See text for details. Contour intervals are .5 K/day for latent heating, and 2 K/day including the contours for ±1, and $\pm.5$ K/day for panels b, c, and d. Negative values are shaded.

Figure A.3. Latent heating rates (a), net diabatic heating (b), net gravity wave heating (c), and the total heating rate (d) for January. See text for details. Contour intervals are .5 K/day for latent heating, and 2 K/day including the contours for ±1, and $\pm.5$ K/day for panels b, c, and d. Negative values are shaded.

Figure A.4. Eliassen-Palm flux divergence due to planetary and synoptic scale waves (F_{PW}) for January. The contour intervals are 2 m/s/day including ±1 and ±.5 m/s/day (values ≤ -2 m/s/day are shaded).

Figure A.4. Eliassen-Palm flux divergence due to planetary and synoptic scale waves (F_{PW}) for January. The contour intervals are 2 m/s/day including ±1 and ±.5 m/s/day (values ≤ -2 m/s/day are shaded).

Figure A.5. Model simulation of CH_4 (ppbv, solid contours) as in Figure A.2 for January and September, along with the model K_{yy} fields depicted in color. The contour interval for CH_4 is 100 ppbv, and the K_{yy} values are in 10^8 cm^2/s.

Figure A.5. Model simulation of CH_4 (ppbv, solid contours) as in Figure A.2 for January and September, along with the model K_{yy} fields depicted in color. The contour interval for CH_4 is 100 ppbv, and the K_{yy} values are in 10^8 cm^2/s.

Figure A.6. Month-latitude sections of the model K_{yy} fields in color, along with $\bar{u}$ overlaid in solid contours, for 68 mbar, 12 mbar, 1.7 mbar, and .1 mbar. The contour interval for $\bar{u}$ is 20 m/s, including ±10 m/s, and the K_{yy} values are in 10^8 cm^2/s.

Figure A.6. Month-latitude sections of the model K_{yy} fields in color, along with $\bar{u}$ overlaid in solid contours, for 68 mbar, 12 mbar, 1.7 mbar, and .1 mbar. The contour interval for $\bar{u}$ is 20 m/s, including ±10 m/s, and the K_{yy} values are in 10^8 cm^2/s.

Figure A.7. Eliassen-Palm flux divergence due to gravity waves (F_{GW}) (a), and the associated model K_{zz} values (b) for January. The contour intervals are, for (a): 20 m/s/day including $\pm 10, \pm 5$, and ±1 m/s/day (negative values are shaded); (b): 20 m^2/s including .02, .03, .1, 1, 5, 10 m^2/s.

Figure A.7. Eliassen-Palm flux divergence due to gravity waves (F_{GW}) (a), and the associated model K_{zz} values (b) for January. The contour intervals are, for (a): 20 m/s/day including $\pm 10, \pm 5$, and ±1 m/s/day (negative values are shaded); (b): 20 m^2/s including .02, .03, .1, 1, 5, 10 m^2/s.

Figure A.8. Month-height sections of $\bar{u}$ and the Eliassen-Palm flux divergence due to Kelvin waves (F_{KW}) at the equator. The contour intervals are for 10 m/s for $\bar{u}$ (negative values are shaded), and .5 m/s/day including .1 m/s/day for F_{KW}.

Figure A.8. Month-height sections of $\bar{u}$ and the Eliassen-Palm flux divergence due to Kelvin waves (F_{KW}) at the equator. The contour intervals are for 10 m/s for $\bar{u}$ (negative values are shaded), and .5 m/s/day including .1 m/s/day for F_{KW}.

Figure A.9. The total Eliassen-Palm flux divergence (F_{TOT}) for January. Contour intervals are 20 m/s/day and include the contours for $\pm 1, \pm 2, \pm 5$, and ±10 m/s/day. Negative values are shaded.

Figure A.9. The total Eliassen-Palm flux divergence (F_{TOT}) for January. Contour intervals are 20 m/s/day and include the contours for $\pm 1, \pm 2, \pm 5$, and ±10 m/s/day. Negative values are shaded.

Table 1. Globally averaged, area weighted annual mean age of air (years) derived from SF_6 (relative to the global mean SF_6 at the ground), at 19, 27, and 35 km, along with the stratospheric steady state lifetimes (years) of $CFCl_3$ and N_2O, for each transport scenario as discussed in the text. Also shown are the lifetimes, along with the 1 standard deviation uncertainties, estimated from ER-2 aircraft data by Volk *et al.* [1997]. We have also included a rough approximation of a global mean age of air, along with a range, derived from OMS balloon SF_6 data. These values are area weighted averages of data taken at 7°S, 35°N, and 65°N. The averages and ranges correspond to observations within ±0.5 km of the altitude indicated.

		Mean Age (yrs)			Lifetime (yrs)	
Scenario	Description	19 km	27 km	35 km	$CFCl_3$	N_2O
A	Base (1999 model)	3.1	4.4	4.9	68	136
B	very weak trop/strat circulation	5.3	7.7	8.4	108	195
C	weak trop/strat circulation	4.3	6.1	6.7	89	166
D	strong trop/strat circulation	2.3	3.3	3.9	55	118
E	very strong trop/strat circulation	1.5	2.2	2.7	40	98
F	stratospheric minimum K_{zz} = .001 m^2/s	3.5	4.8	5.3	71	139
G	stratospheric minimum K_{zz} = .1 m^2/s	2.6	3.9	4.4	62	130
H	stratospheric minimum K_{zz} = 1 m^2/s	1.0	1.8	2.3	34	96
I	weak mesospheric gravity wave drag, K_{zz}	3.2	4.5	5.1	69	142
J	strong mesospheric gravity wave drag, K_{zz}	2.9	4.1	4.5	63	121
K	K_{yy}/5 (above tropopause)	2.3	2.6	2.8	49	98
L	K_{yy}/2 (above tropopause)	2.6	3.3	3.6	56	112
M	K_{yy}*2 (above tropopause)	3.8	6.2	7.2	86	178
N	K_{yy}*5 (above tropopause)	4.8	9.6	11.5	120	262
O	K_{yy}/5 + wave drive/5 (above tropopause)	3.4	3.7	4.0	66	126
P	K_{yy}*5 + wave drive*5 (above tropopause)	1.2	2.4	2.8	38	93
Q	small tropical stratospheric K_{yy}	3.0	3.7	3.7	62	122
R	large cross-tropopause K_{yy}	3.2	4.6	5.1	69	137
S	combination, very long strat residence time (B+F+N)	9.6	18.0	20.2	231	461
T	combination, long strat residence time (C+F+M)	6.4	9.8	11.0	129	243
U	combination, short strat residence time (D+G+L)	1.8	2.4	2.8	45	99
V	combination, very short strat residence time (E+H+K)	0.7	1.1	1.4	27	77
W	1995 model	1.7	2.9	3.4	46	111
	average of OMS SF_6 profiles	2.1±0.7	5.1±0.4	...		
	Volk *et al.* [1997] observational estimates				45±7	122±24

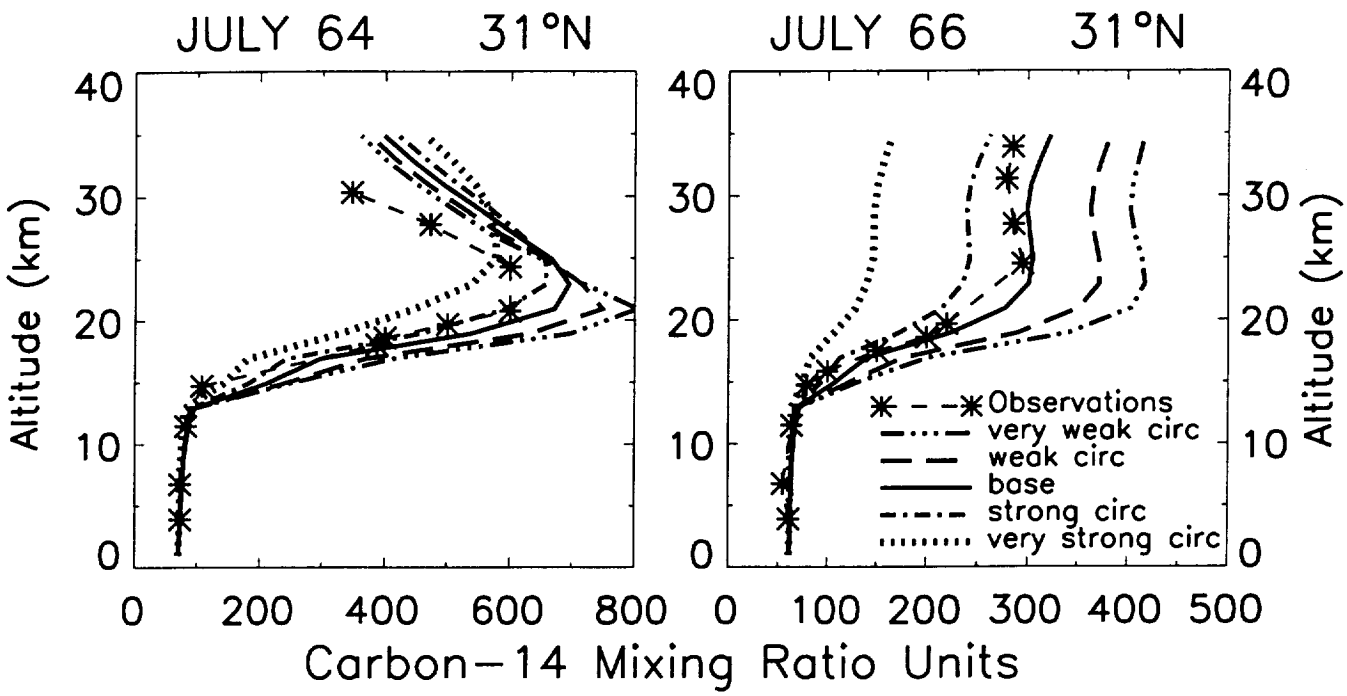
JULY 64 31°N
JULY 66 31°N
Altitude (km)
Altitude (km)
0
10
20
30
40
0 200 400 600 800
0 100 200 300 400 500
Carbon−14 Mixing Ratio Units
Observations
very weak circ
weak circ
base
strong circ
very strong circ

FIGURE 1

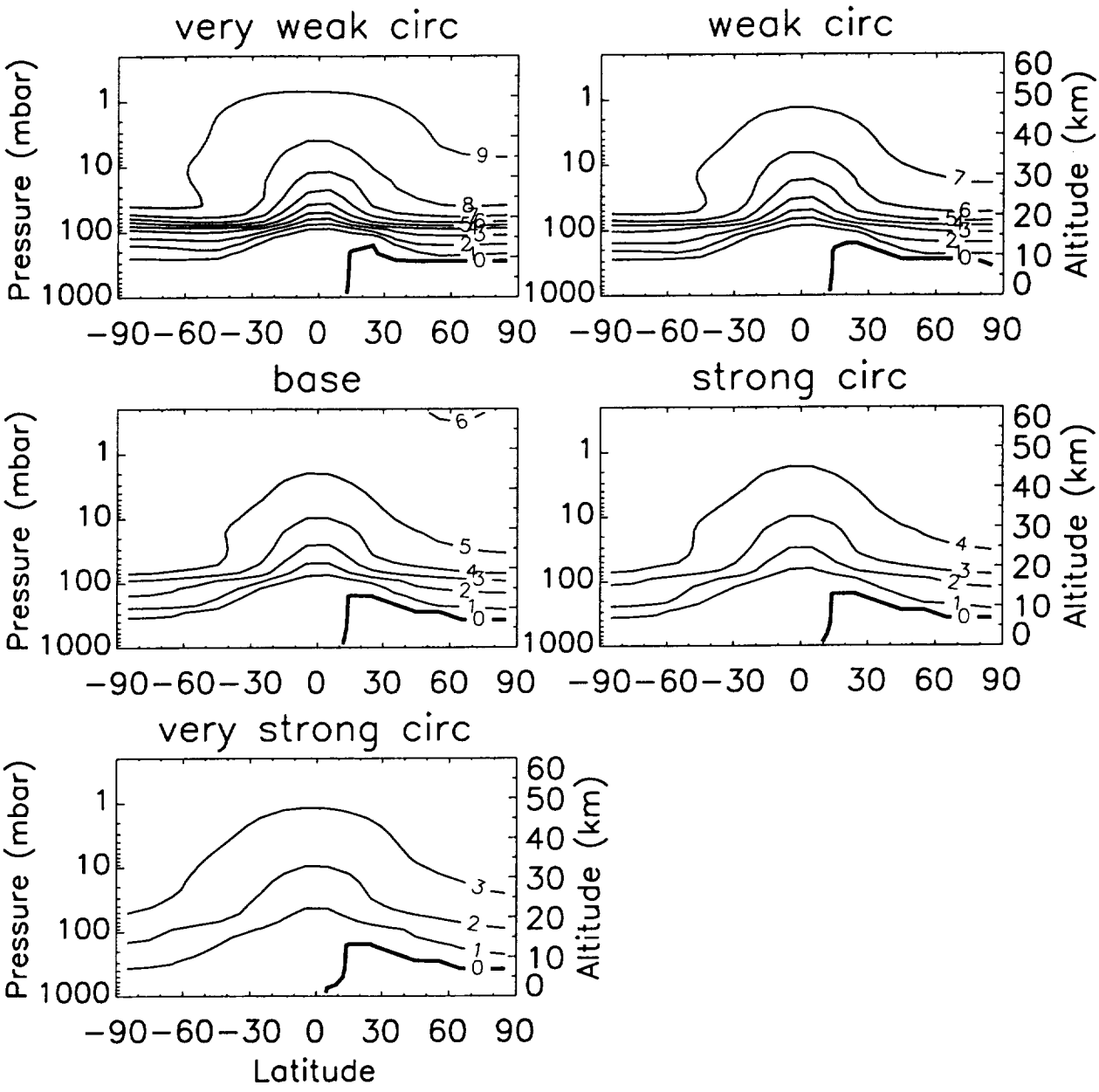
very weak circ
weak circ
base
strong circ
very strong circ
Pressure (mbar)
Altitude (km)
Latitude
1
10
100
1000
0
10
20
30
40
50
60
−90 −60 −30 0 30 60 90

Fig 2

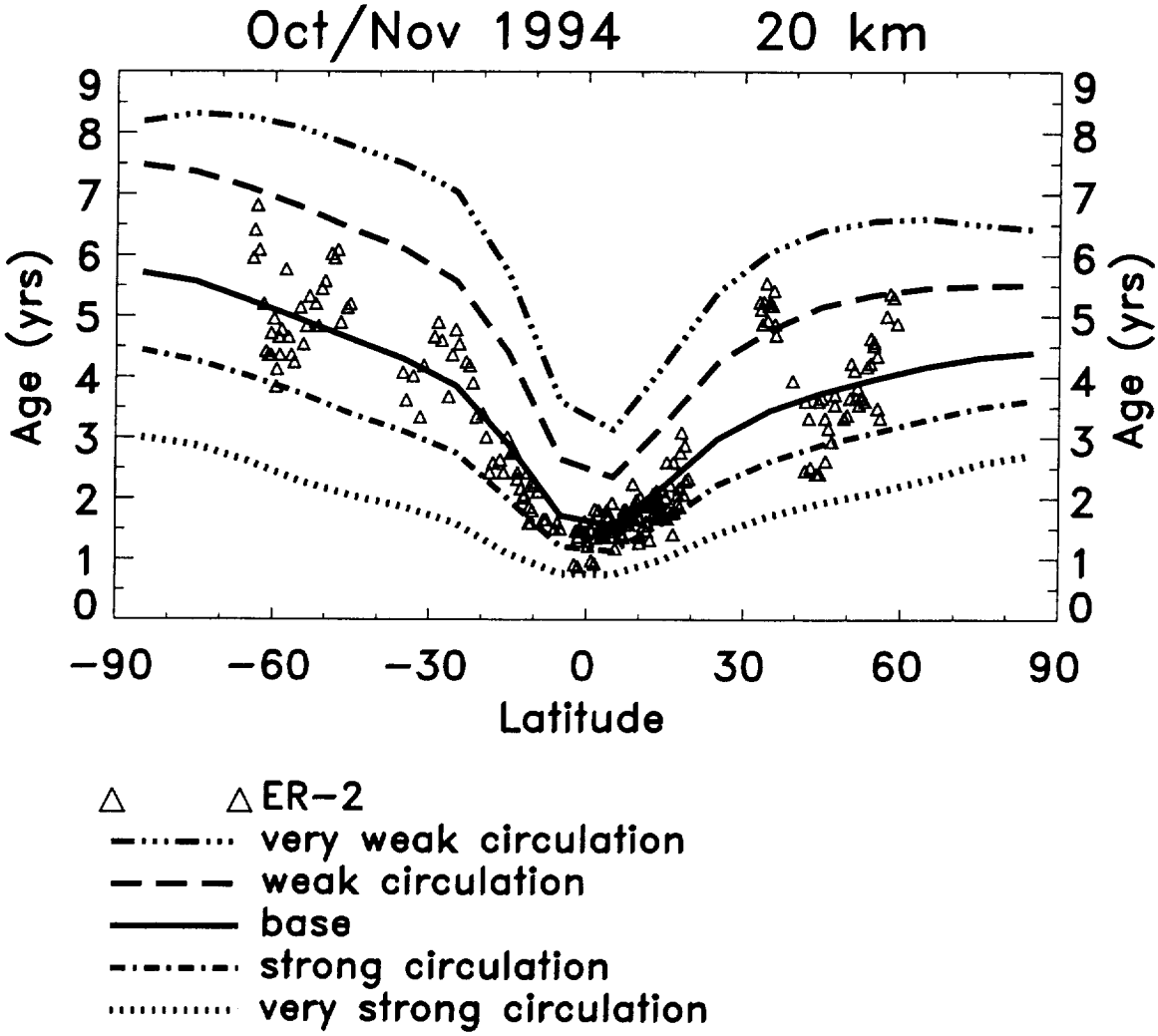
Oct/Nov 1994 20 km
Age (yrs)
Age (yrs)
Latitude
−90 −60 −30 0 30 60 90
0 1 2 3 4 5 6 7 8 9
△ △ ER−2
very weak circulation
weak circulation
base
strong circulation
very strong circulation

FIG 3

Fig 3

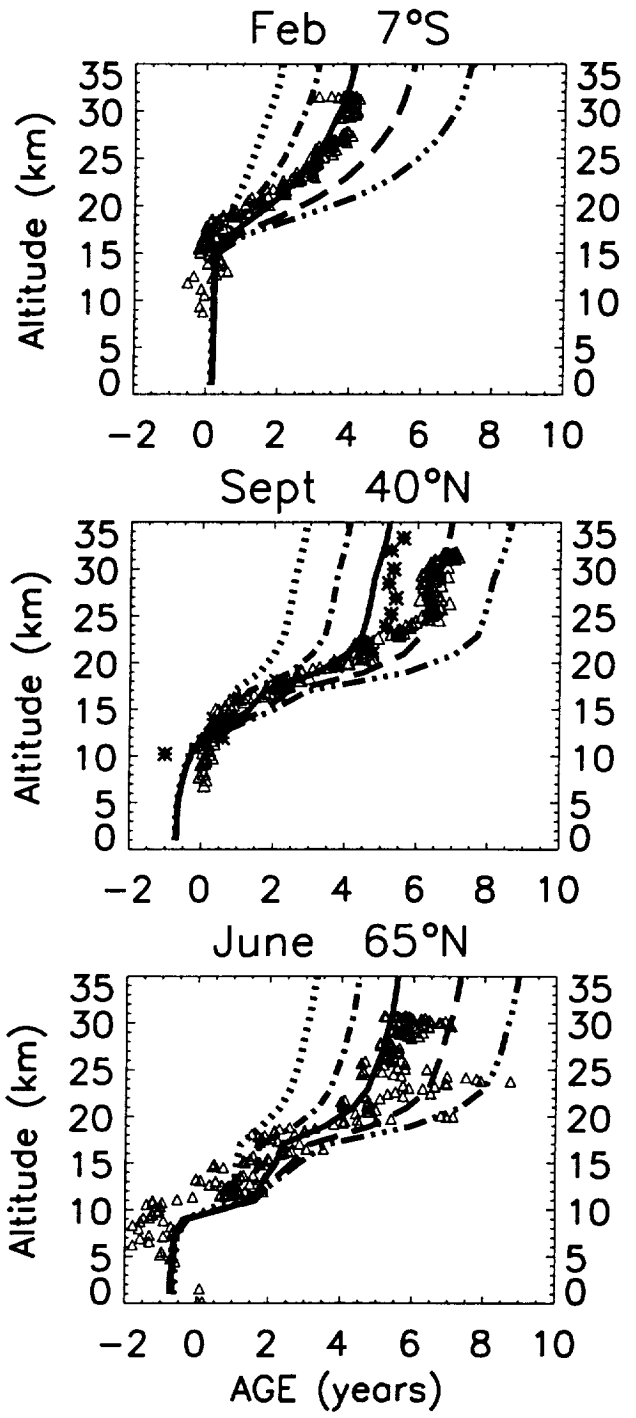
Feb 7°S
Sept 40°N
June 65°N
Altitude (km)
AGE (years)
35
30
25
20
15
10
5
0
−2
0
2
4
6
8
10
✳Harnisch et al., 1996 SF6
△OMS SF6
very weak circulation
weak circulation
base
strong circulation
very strong circulation

Fig 4

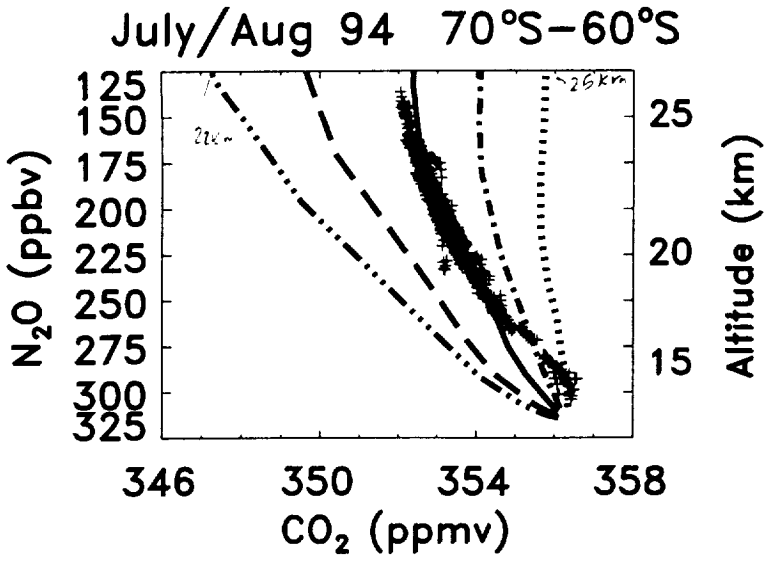
July/Aug 94 70°S–60°S
125
150
175
200
225
250
275
300
325
N_2O (ppbv)
25
20
15
Altitude (km)
346
350
354
358
CO_2 (ppmv)
ER–2
very weak circulation
weak circulation
base
strong circulation
very strong circulation

Fig. 5

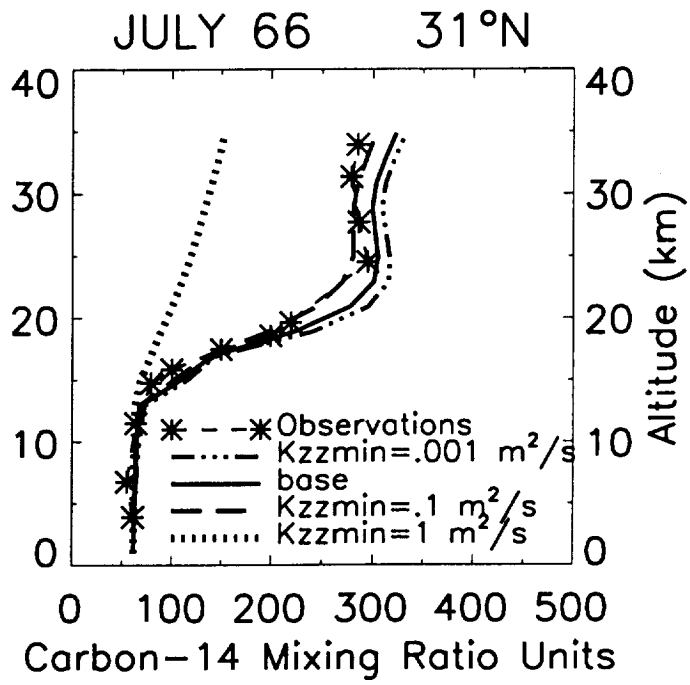
JULY 66 31°N
40
30
20
10
0
Altitude (km)
Observations
Kzzmin=.001 m²/s
base
Kzzmin=.1 m²/s
Kzzmin=1 m²/s
0 100 200 300 400 500
Carbon-14 Mixing Ratio Units

FIGURE 6

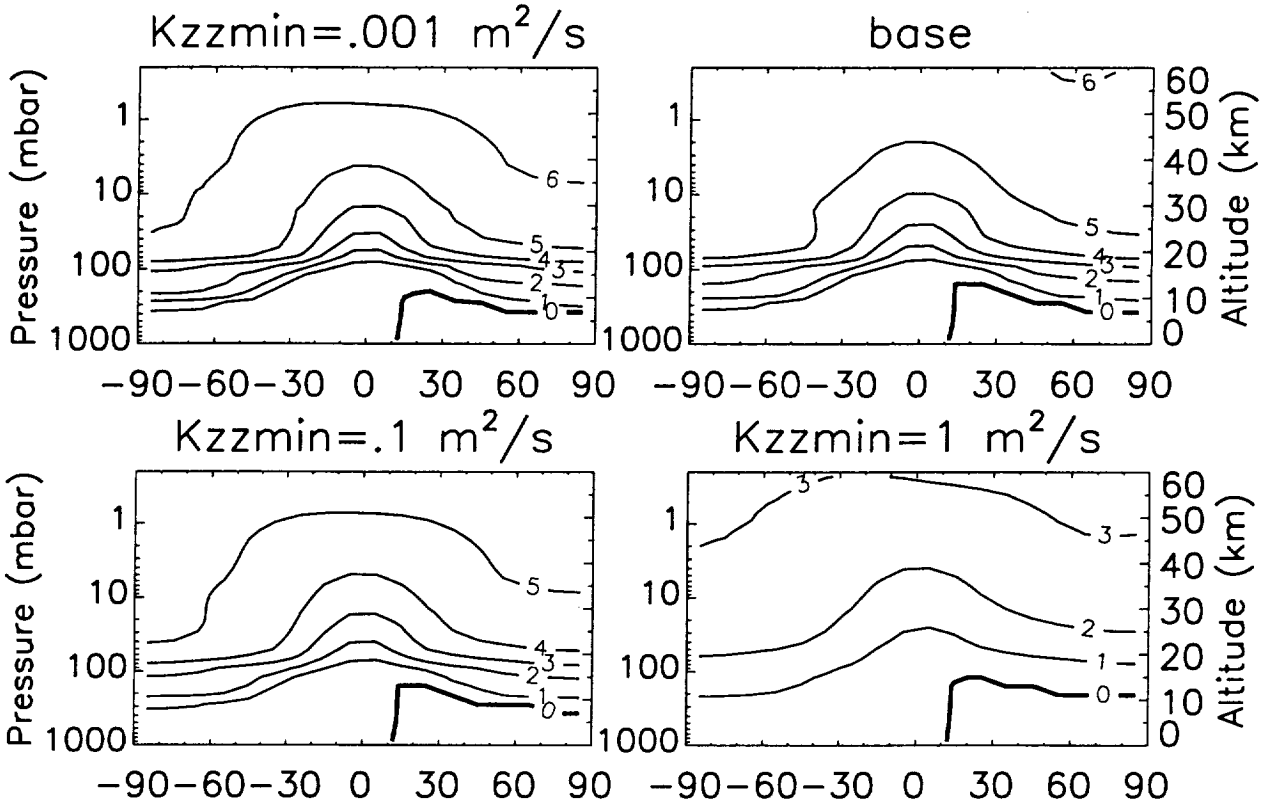
Kzzmin=.001 m²/s
base
Kzzmin=.1 m²/s
Kzzmin=1 m²/s
Pressure (mbar)
Altitude (km)
1
10
100
1000
0
10
20
30
40
50
60
-90 -60 -30 0 30 60 90
6
5
4
3
2
1
0

Fig 7

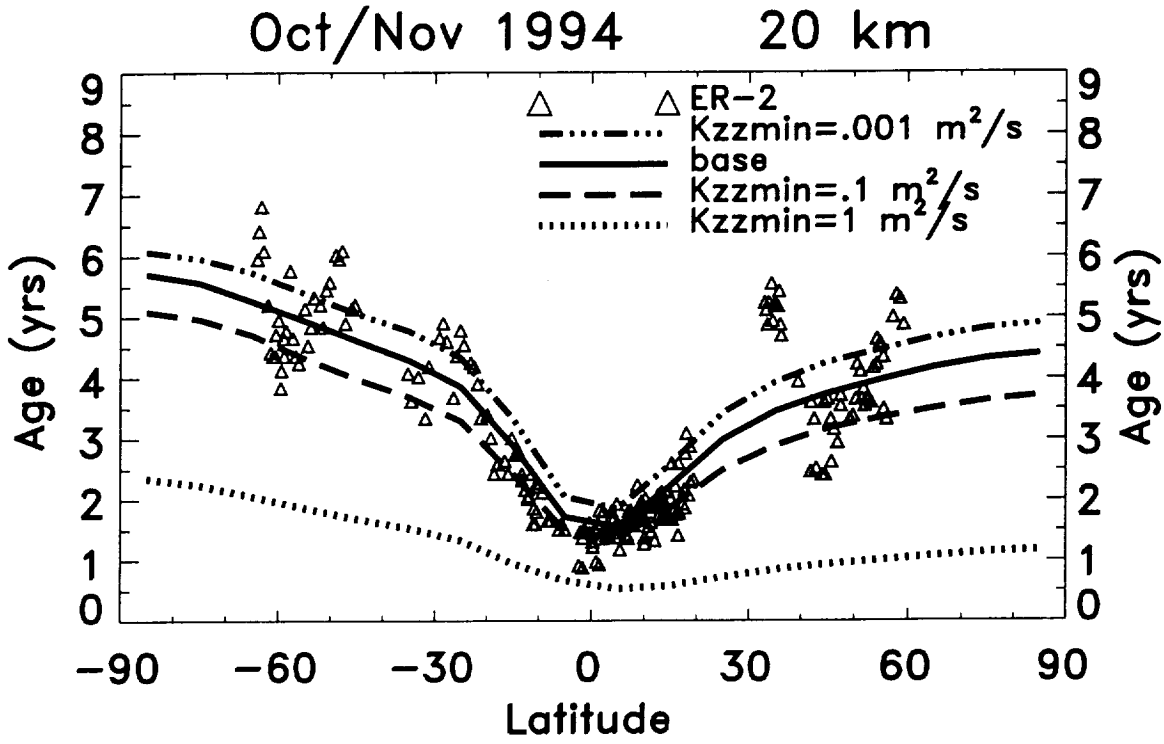
Oct/Nov 1994 20 km
ER-2
Kzzmin=.001 m²/s
base
Kzzmin=.1 m²/s
Kzzmin=1 m²/s
Age (yrs)
Age (yrs)
Latitude
9
8
7
6
5
4
3
2
1
0
−90
−60
−30
0
30
60
90

Fig 8

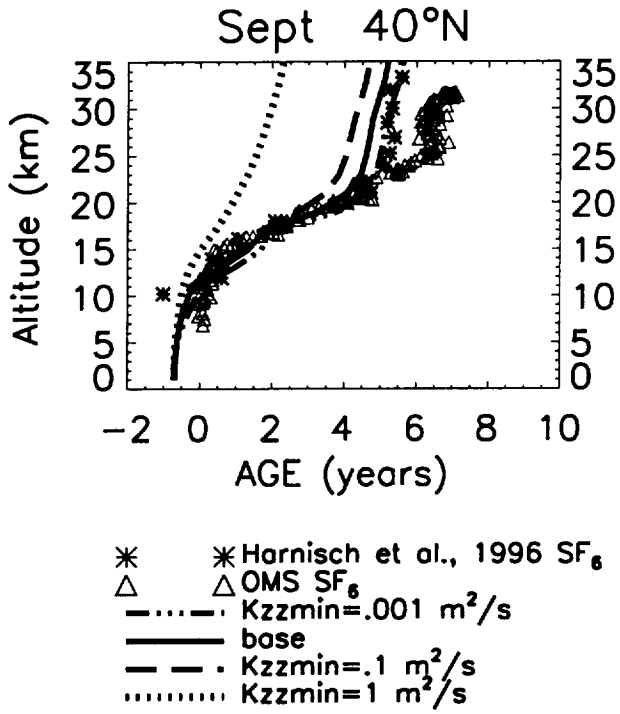
Sept 40°N
Altitude (km)
35
30
25
20
15
10
5
0
−2 0 2 4 6 8 10
AGE (years)
Harnisch et al., 1996 SF6
OMS SF6
Kzzmin=.001 m²/s
base
Kzzmin=.1 m²/s
Kzzmin=1 m²/s

FIGURE 9

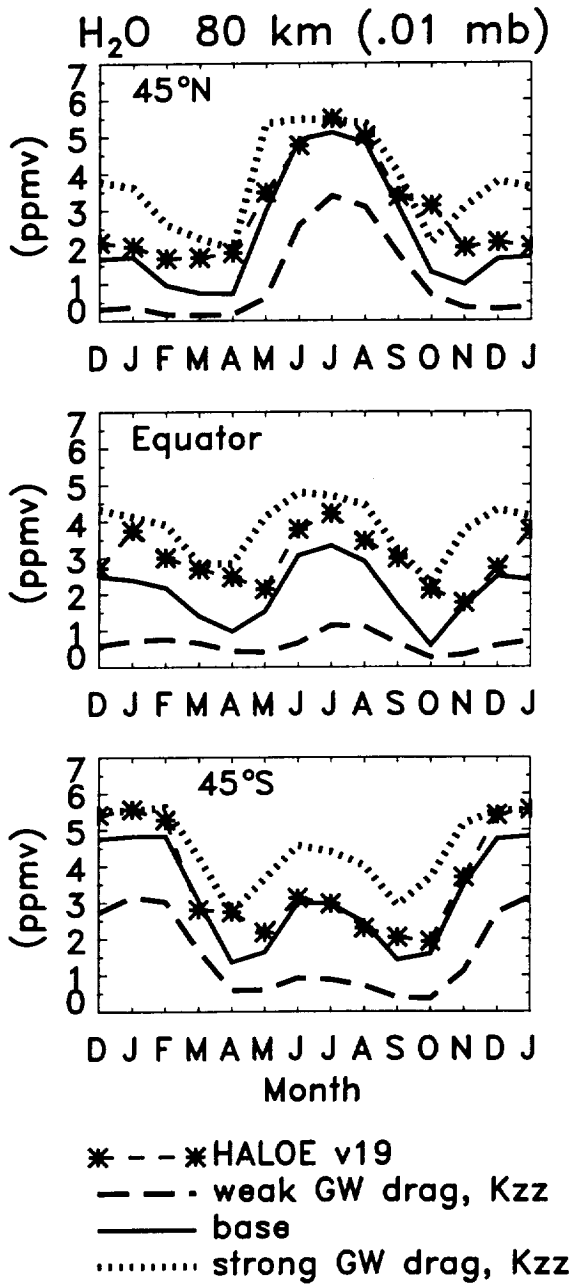
H_2O 80 km (.01 mb)
45°N
Equator
45°S
(ppmv)
0 1 2 3 4 5 6 7
D J F M A M J J A S O N D J
Month
HALOE v19
weak GW drag, Kzz
base
strong GW drag, Kzz

Figure 10

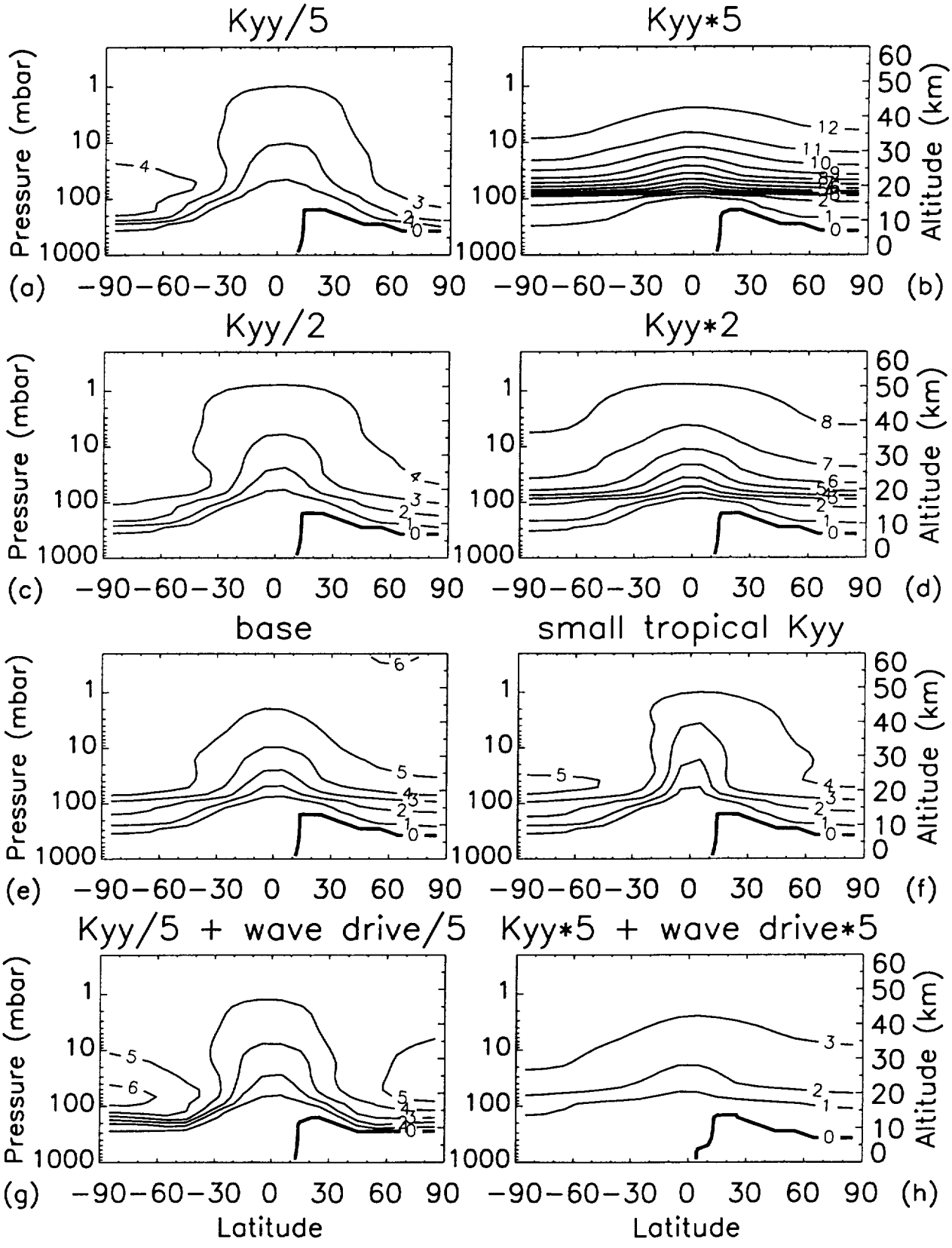
Kyy/5
Kyy*5
Kyy/2
Kyy*2
base
small tropical Kyy
Kyy/5 + wave drive/5
Kyy*5 + wave drive*5
Pressure (mbar)
Altitude (km)
Latitude
(a)
(b)
(c)
(d)
(e)
(f)
(g)
(h)

Fig. 11

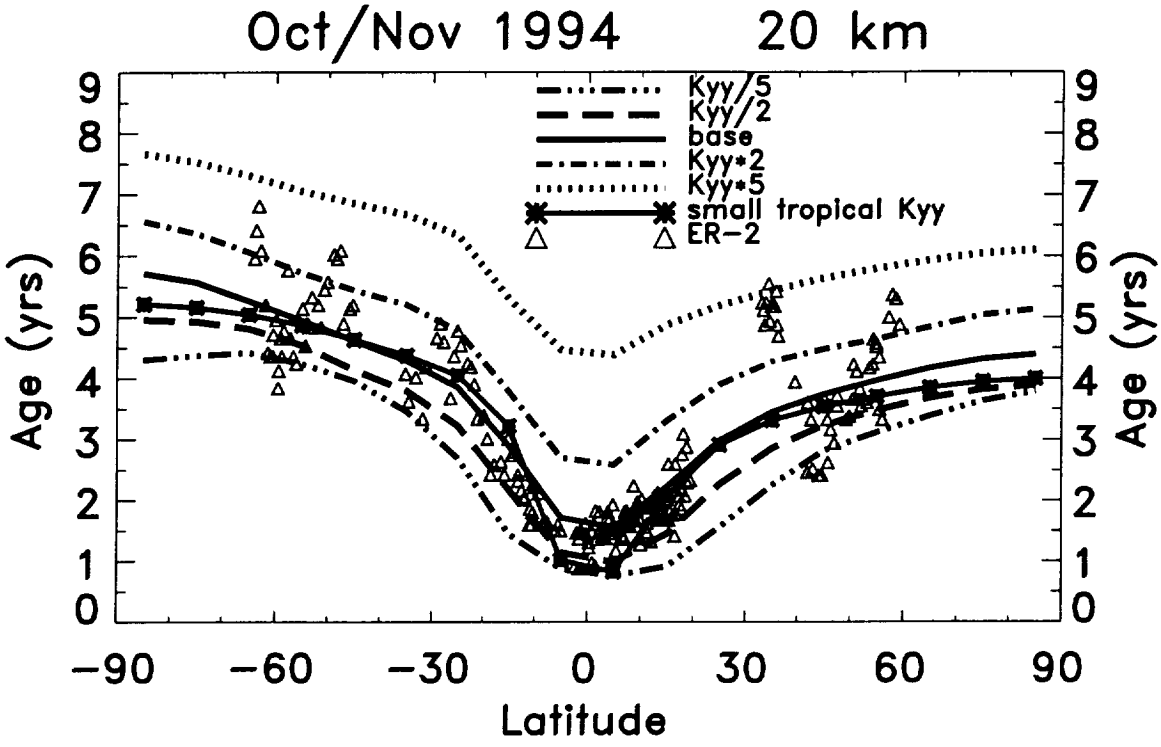
Oct/Nov 1994 20 km
Kyy/5
Kyy/2
base
Kyy*2
Kyy*5
small tropical Kyy
ER-2
Age (yrs)
Age (yrs)
Latitude
9
8
7
6
5
4
3
2
1
0
−90
−60
−30
0
30
60
90

Fig. 12

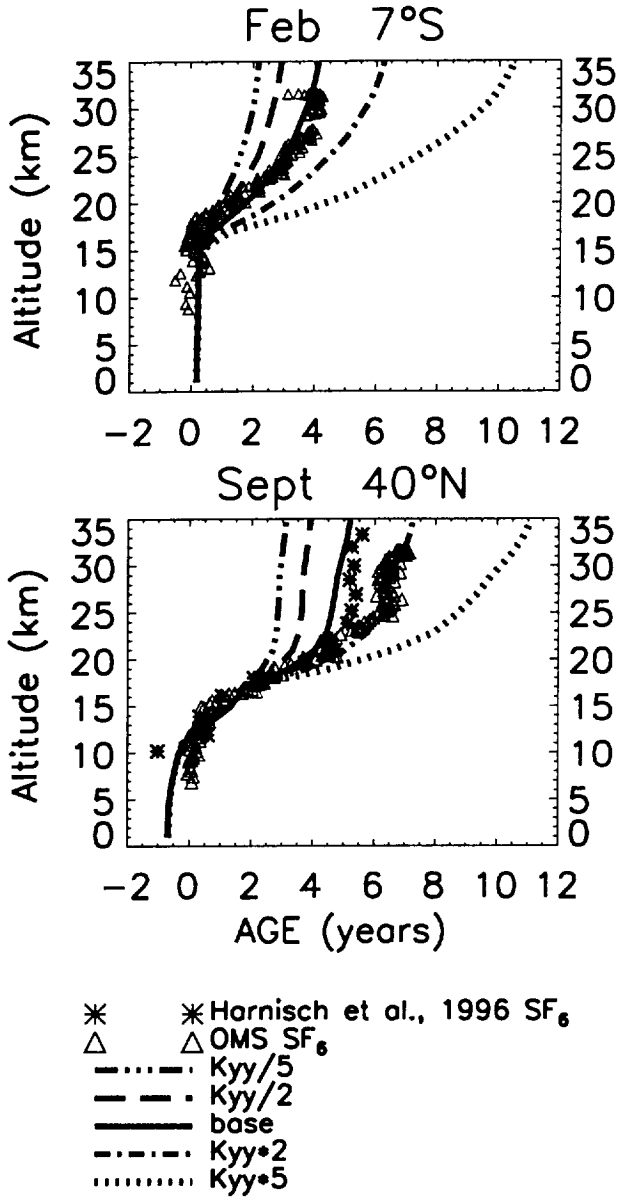
Feb 7°S
Sept 40°N
Altitude (km)
AGE (years)
Harnisch et al., 1996 SF6
OMS SF6
Kyy/5
Kyy/2
base
Kyy*2
Kyy*5

FIGURE 13

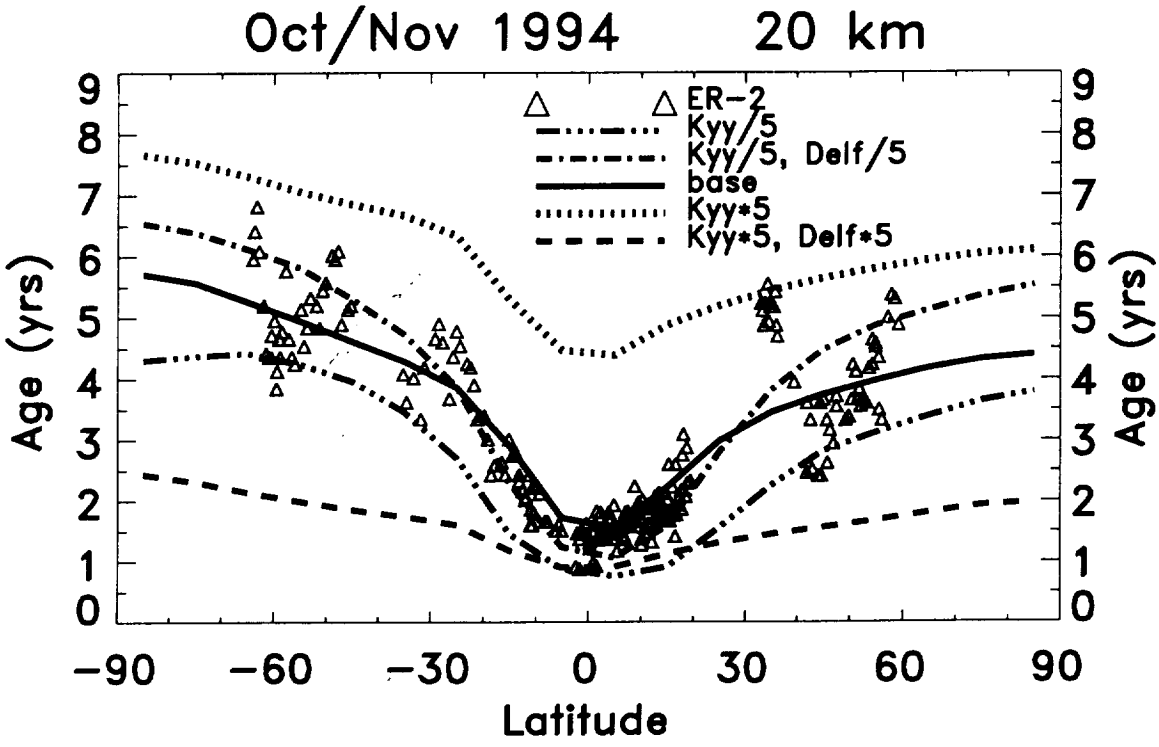
Oct/Nov 1994 20 km
ER-2
Kyy/5
Kyy/5, Delf/5
base
Kyy*5
Kyy*5, Delf*5
Age (yrs)
Age (yrs)
Latitude
9
8
7
6
5
4
3
2
1
0
−90
−60
−30
0
30
60
90

Fig 14

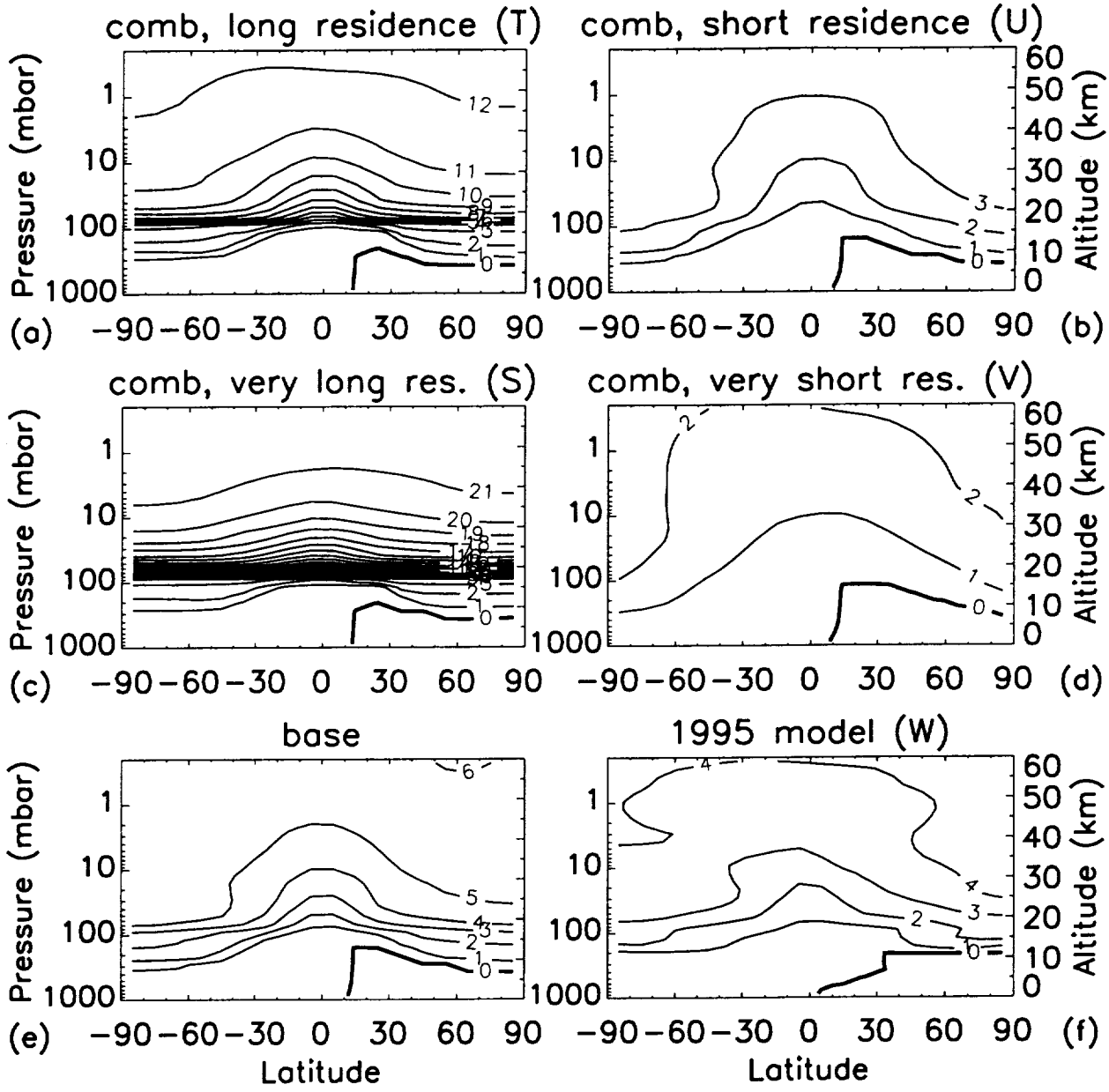
comb, long residence (T)
comb, short residence (U)
comb, very long res. (S)
comb, very short res. (V)
base
1995 model (W)
Pressure (mbar)
Altitude (km)
Latitude
(a)
(b)
(c)
(d)
(e)
(f)

FIGURE 15

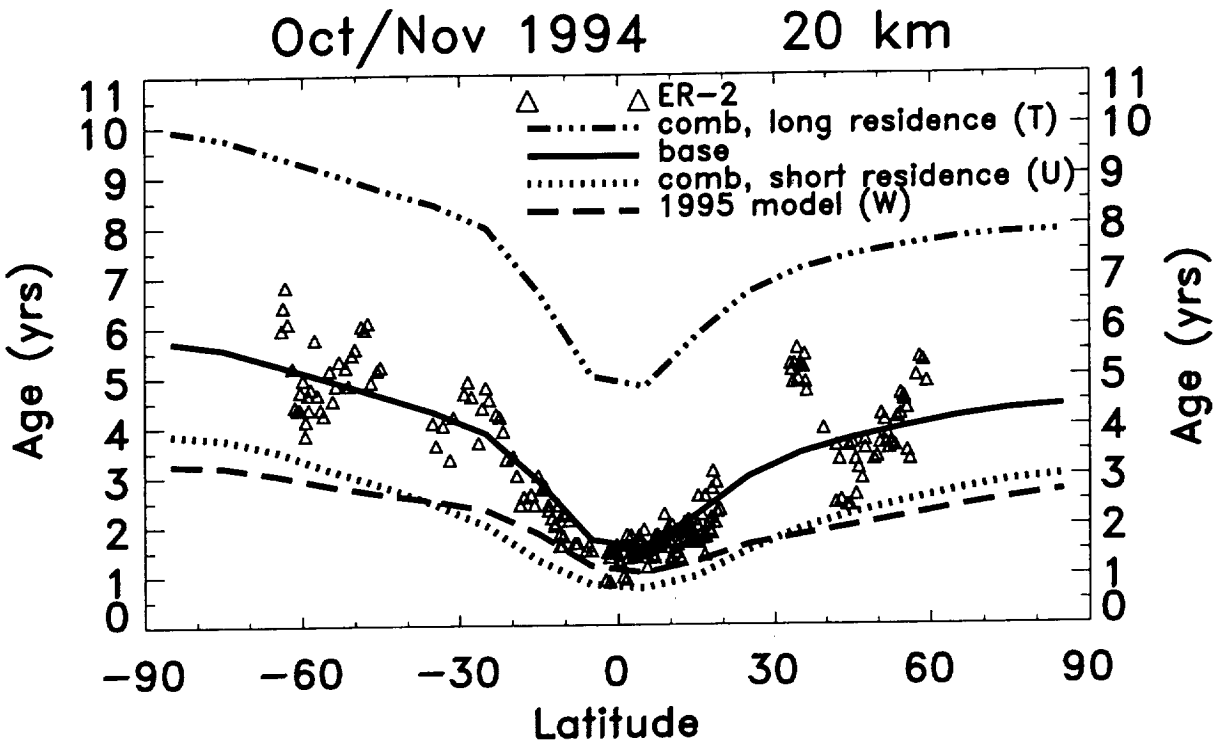
Oct/Nov 1994 20 km
ER-2
comb, long residence (T)
base
comb, short residence (U)
1995 model (W)
Age (yrs)
Age (yrs)
Latitude
−90
−60
−30
0
30
60
90
0
1
2
3
4
5
6
7
8
9
10
11

FIGURE 16

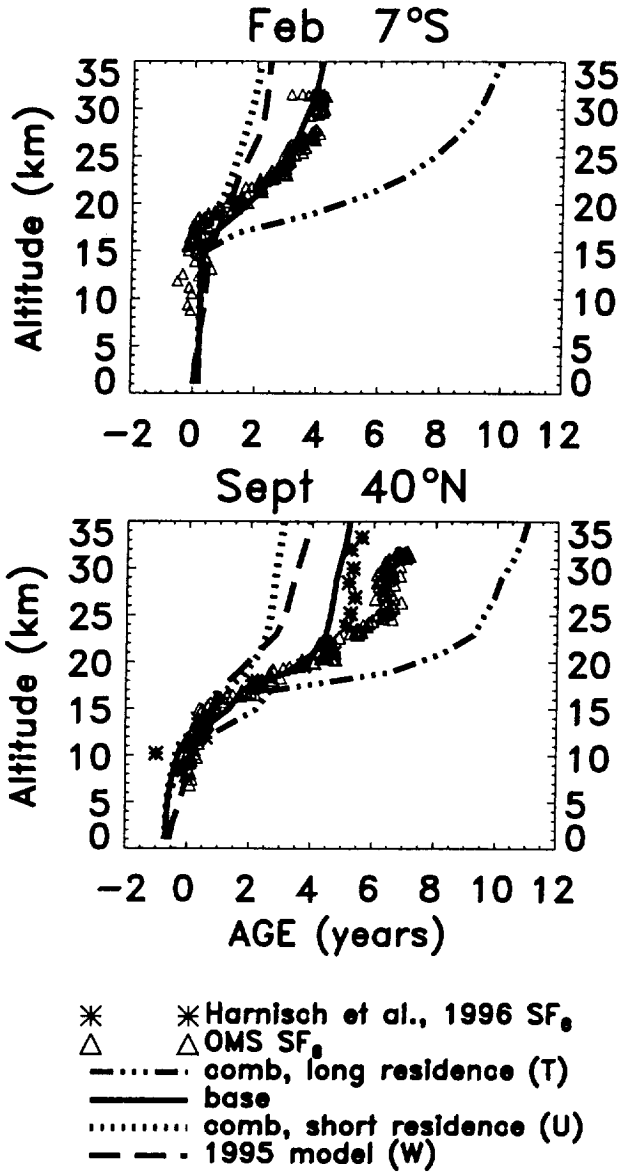
Feb 7°S
Sept 40°N
Altitude (km)
AGE (years)
35
30
25
20
15
10
5
0
−2 0 2 4 6 8 10 12
Harnisch et al., 1996 SF6
OMS SF6
comb, long residence (T)
base
comb, short residence (U)
1995 model (W)

FIGURE 17

27 km global/annual avg

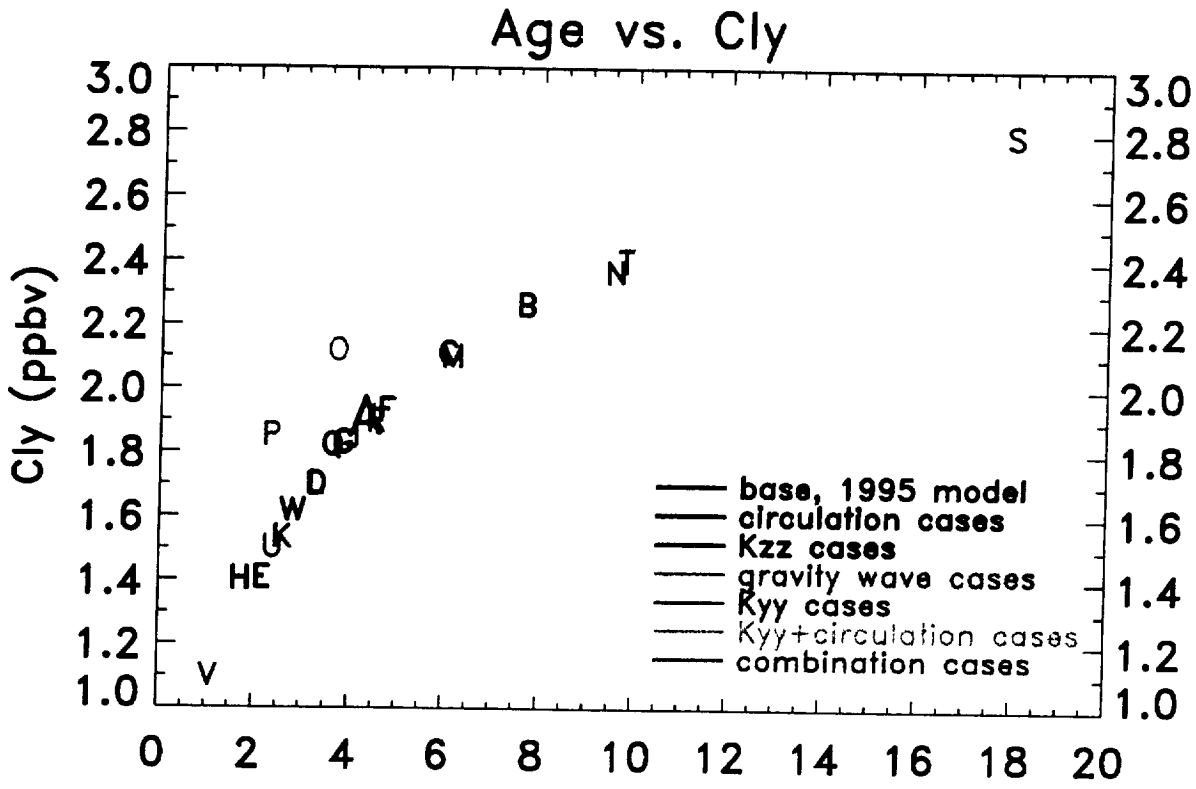

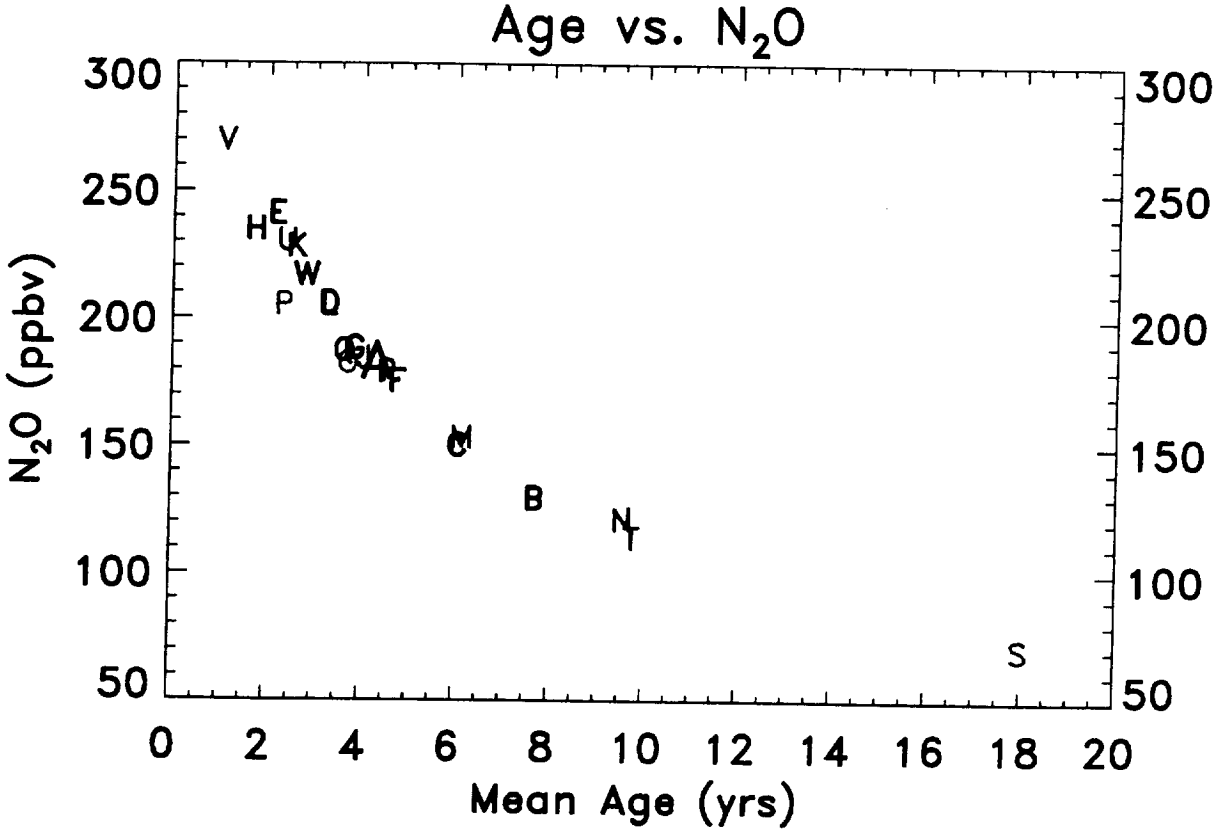

FIG. 18

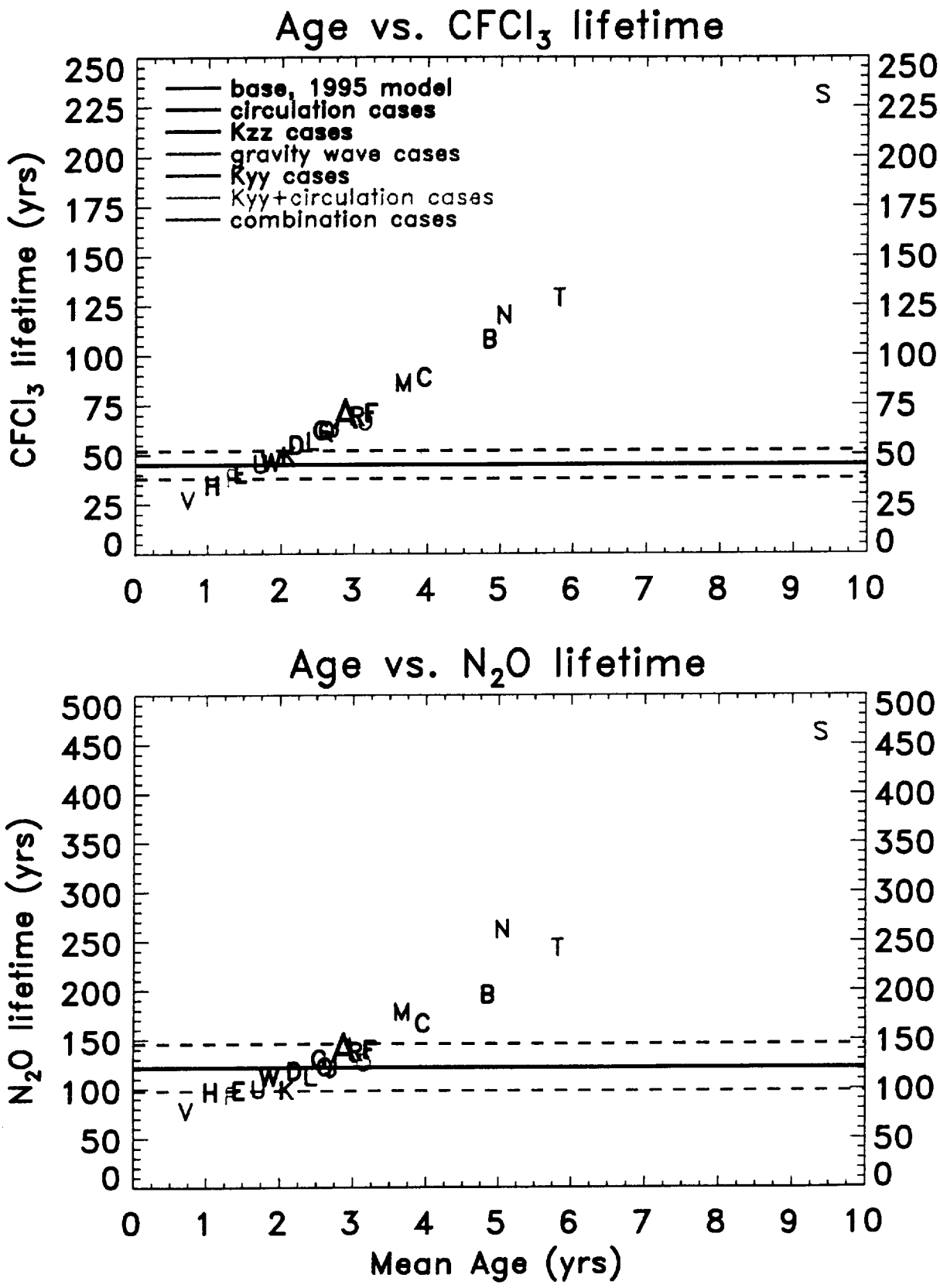
global/annual/stratospheric (levs 7–23) avg
Age vs. $CFCl_3$ lifetime
base, 1995 model
circulation cases
Kzz cases
gravity wave cases
Kyy cases
Kyy+circulation cases
combination cases
$CFCl_3$ lifetime (yrs)
Age vs. N_2O lifetime
N_2O lifetime (yrs)
Mean Age (yrs)

FIG. 19

JANUARY

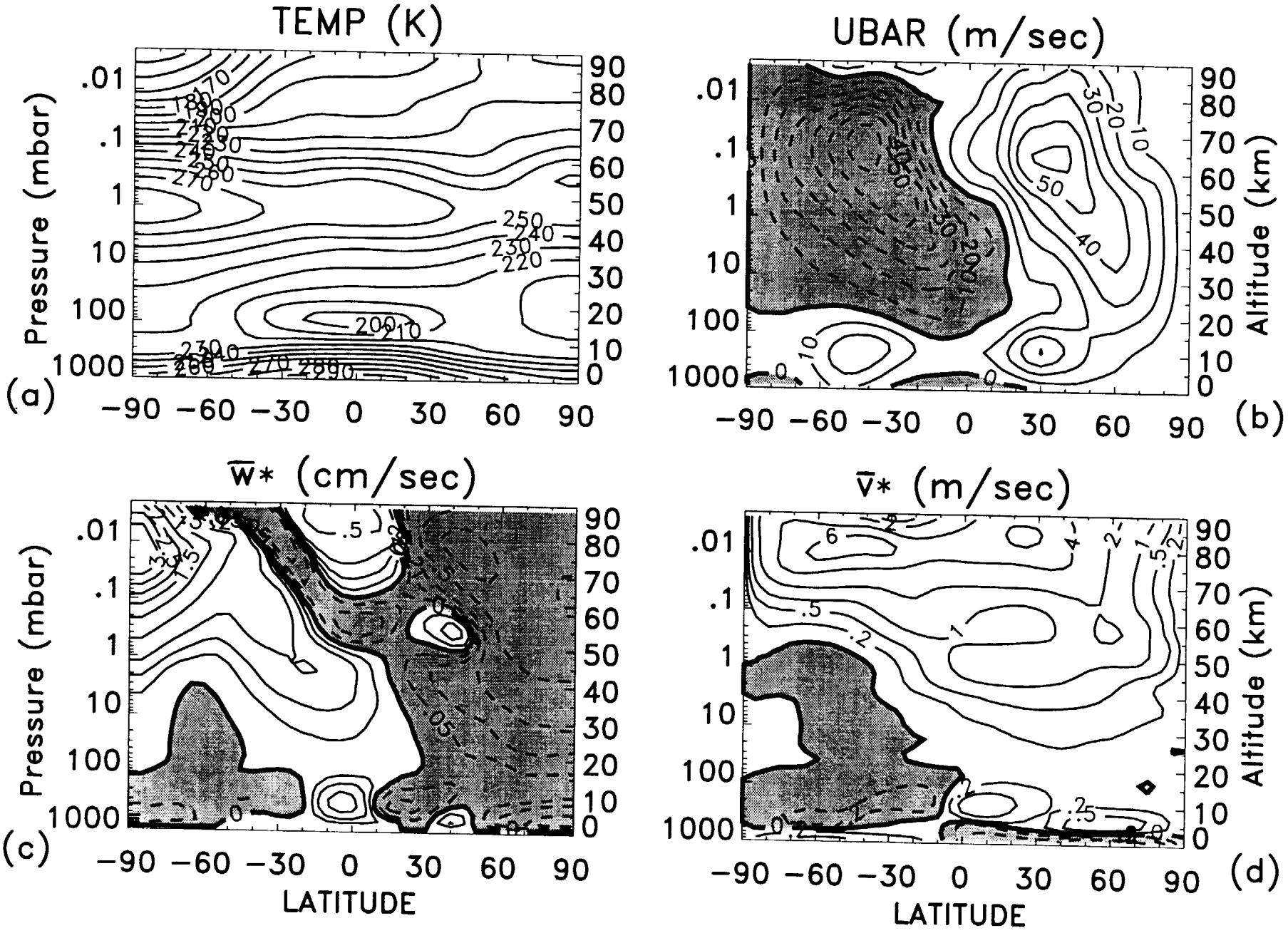

FIG A.1

Circulation, CH_4 (ppbv)

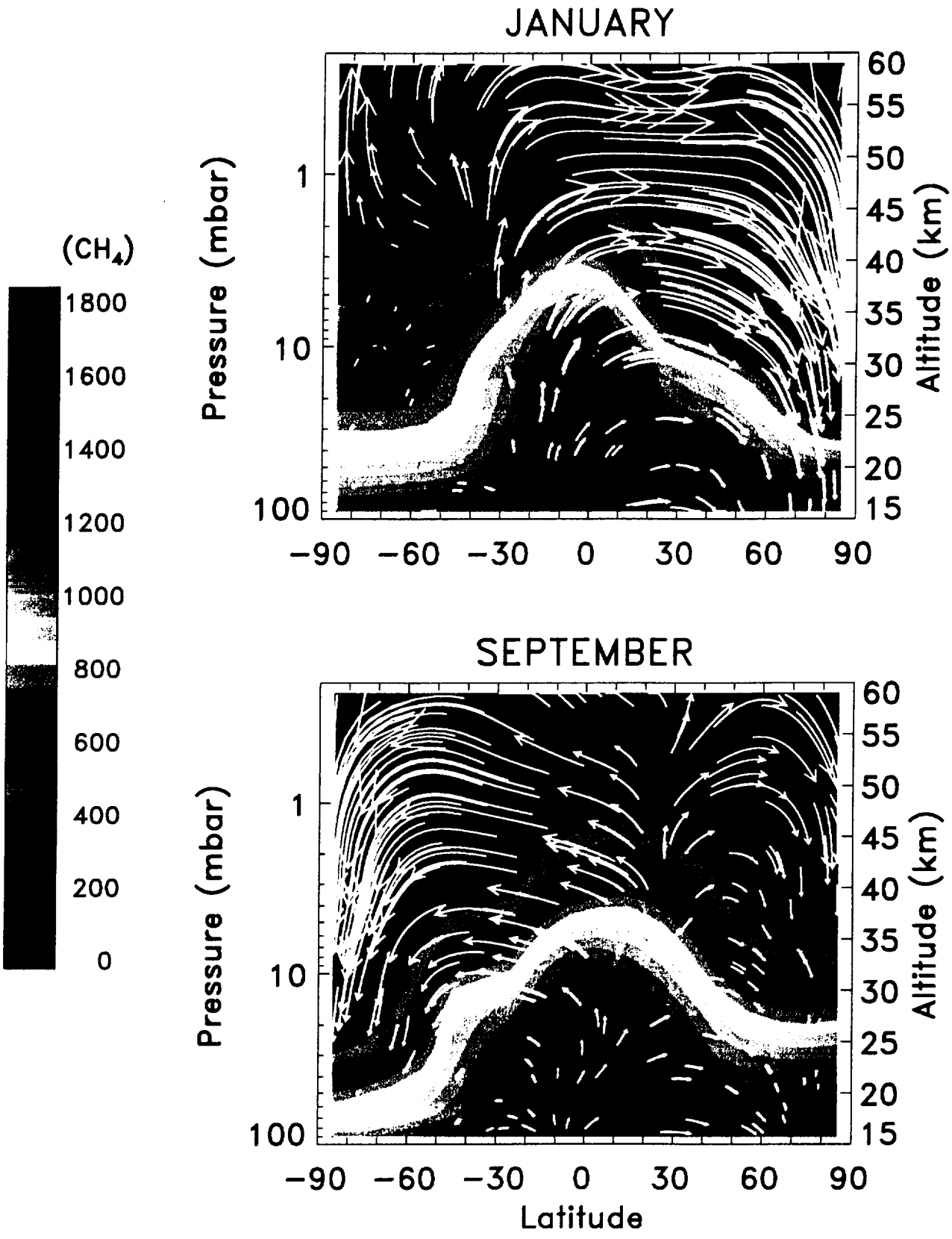

FIG A.2

JANUARY

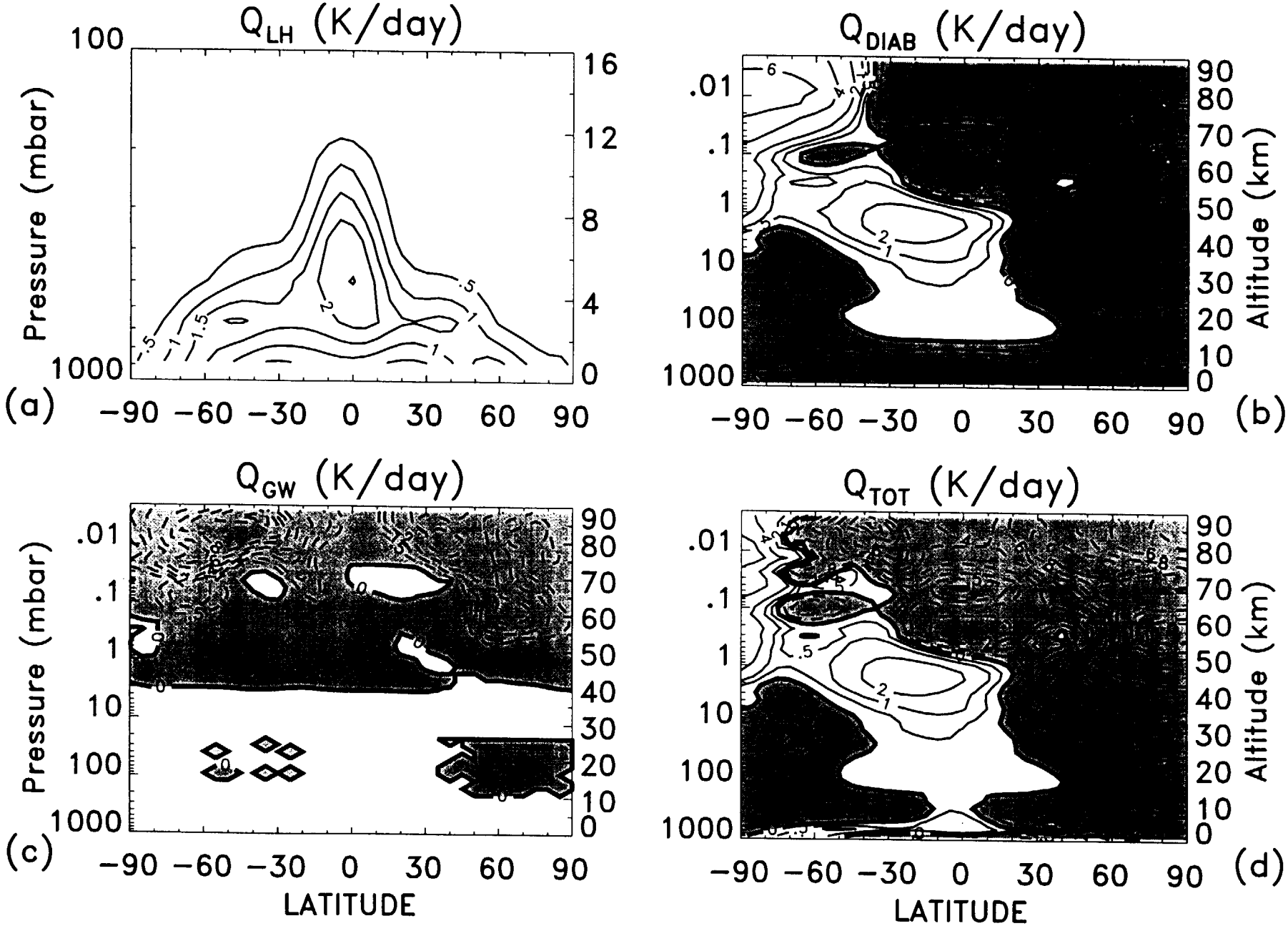

FIG A.3

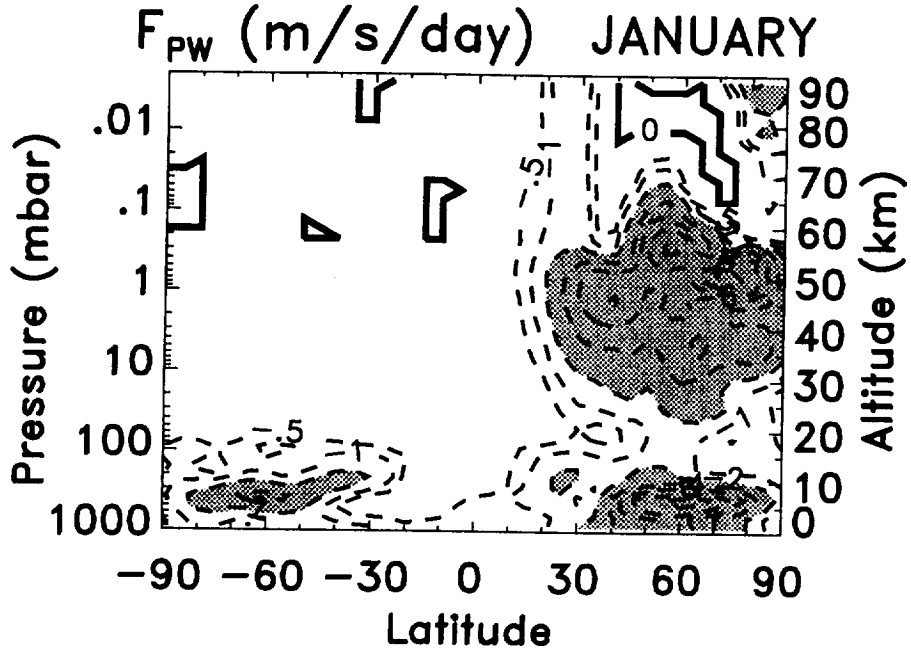
F_PW (m/s/day) JANUARY
Pressure (mbar)
.01
.1
1
10
100
1000
Altitude (km)
90
80
70
60
50
40
30
20
10
0
−90 −60 −30 0 30 60 90
Latitude
.5
1
0
2

FIGURE A.4

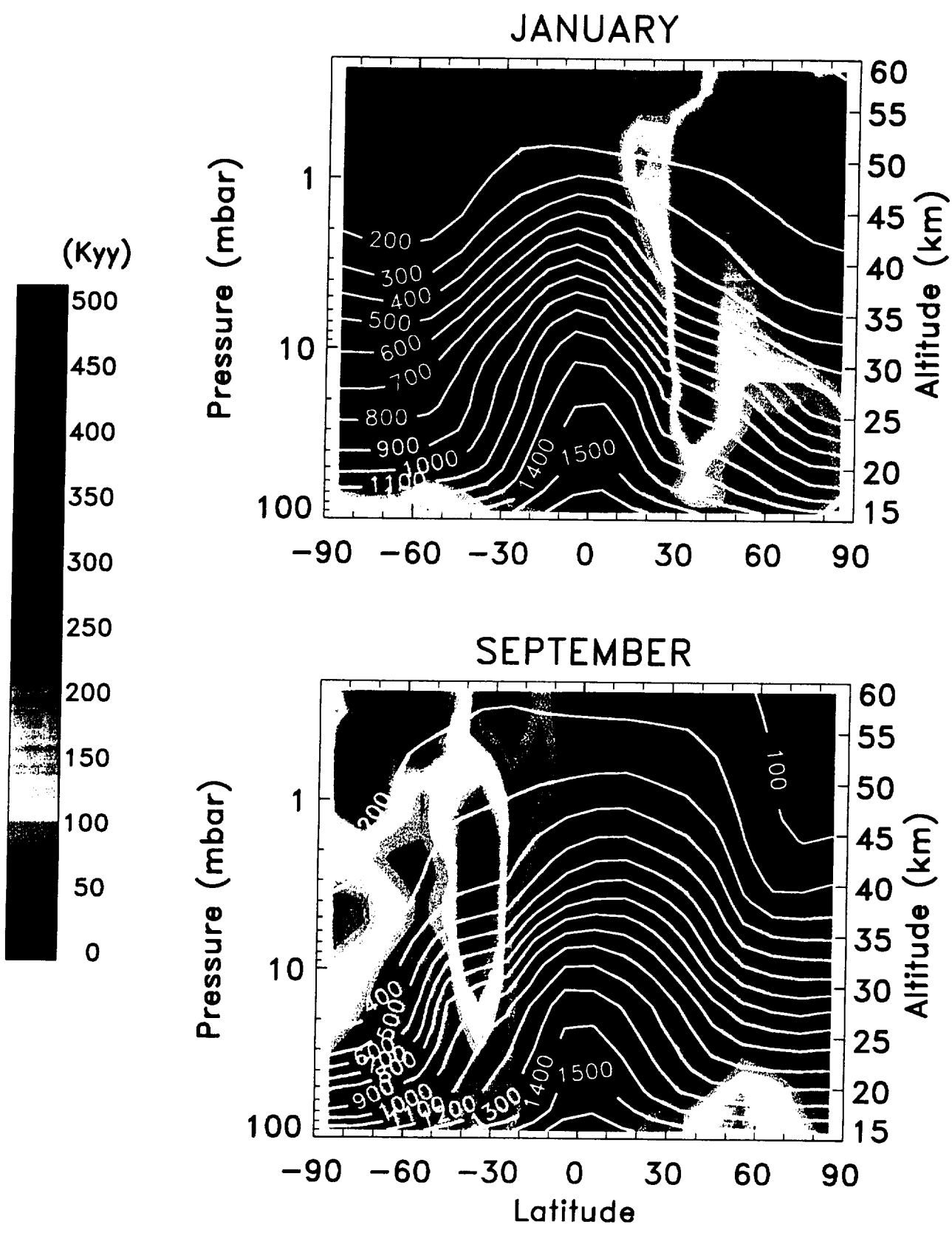
Kyy (10^8 cm^2/sec), CH_4 (ppbv)
JANUARY
SEPTEMBER
(Kyy)
500
450
400
350
300
250
200
150
100
50
0
Pressure (mbar)
Altitude (km)
Latitude
1
10
100
60
55
50
45
40
35
30
25
20
15
−90
−60
−30
0
30
60
90
200
300
400
500
600
700
800
900
1000
1100
1400
1500

FIG. A.5 - West

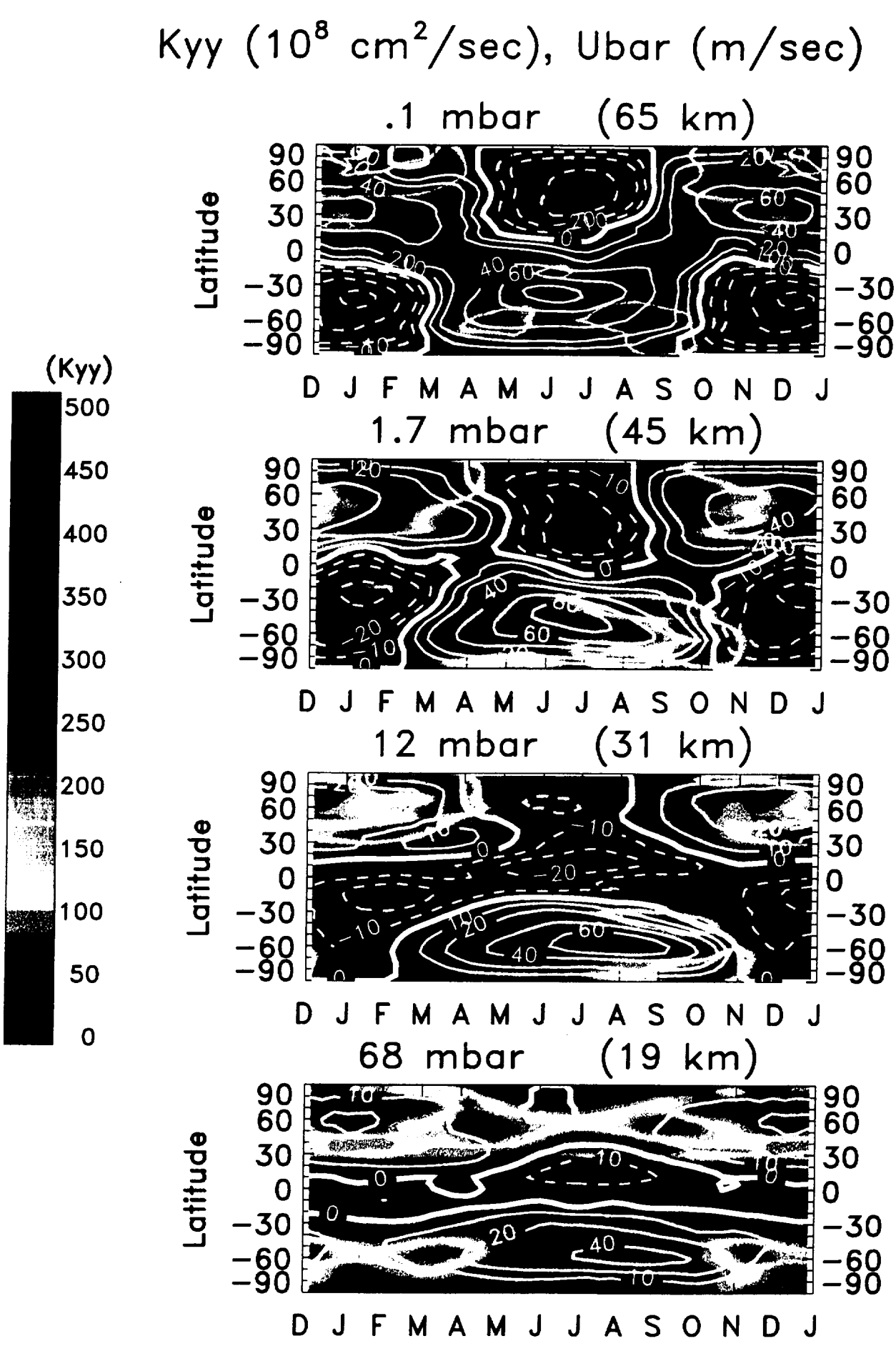
Kyy (10^8 cm^2/sec), Ubar (m/sec)
.1 mbar (65 km)
1.7 mbar (45 km)
12 mbar (31 km)
68 mbar (19 km)
Latitude
90
60
30
0
−30
−60
−90
D J F M A M J J A S O N D J
(Kyy)
500
450
400
350
300
250
200
150
100
50
0

FIG A.6
- best

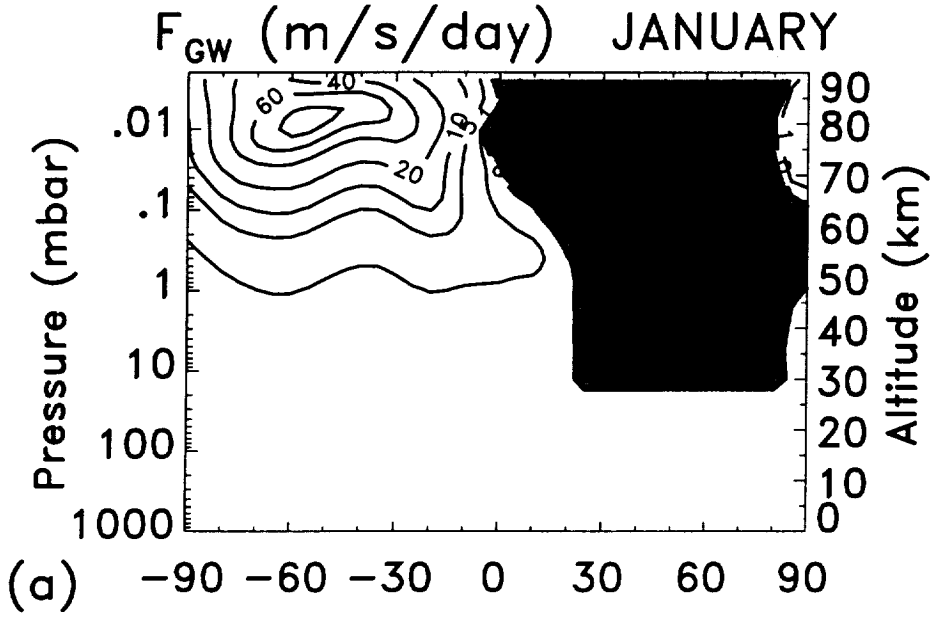
F_{GW} (m/s/day) JANUARY
Pressure (mbar)
.01
.1
1
10
100
1000
Altitude (km)
90
80
70
60
50
40
30
20
10
0
60
40
20
10
(a)
−90 −60 −30 0 30 60 90

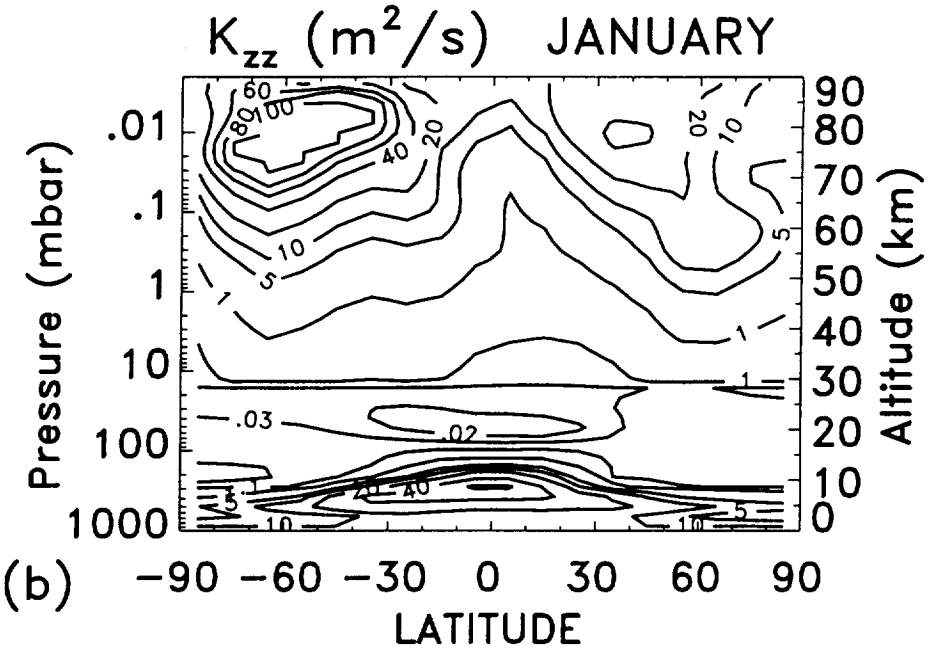
K_{zz} (m^2/s) JANUARY
Pressure (mbar)
.01
.1
1
10
100
1000
Altitude (km)
90
80
70
60
50
40
30
20
10
0
60
80
100
40
20
10
5
1
.03
.02
(b)
−90 −60 −30 0 30 60 90
LATITUDE

FIGURE A.7

EQUATOR

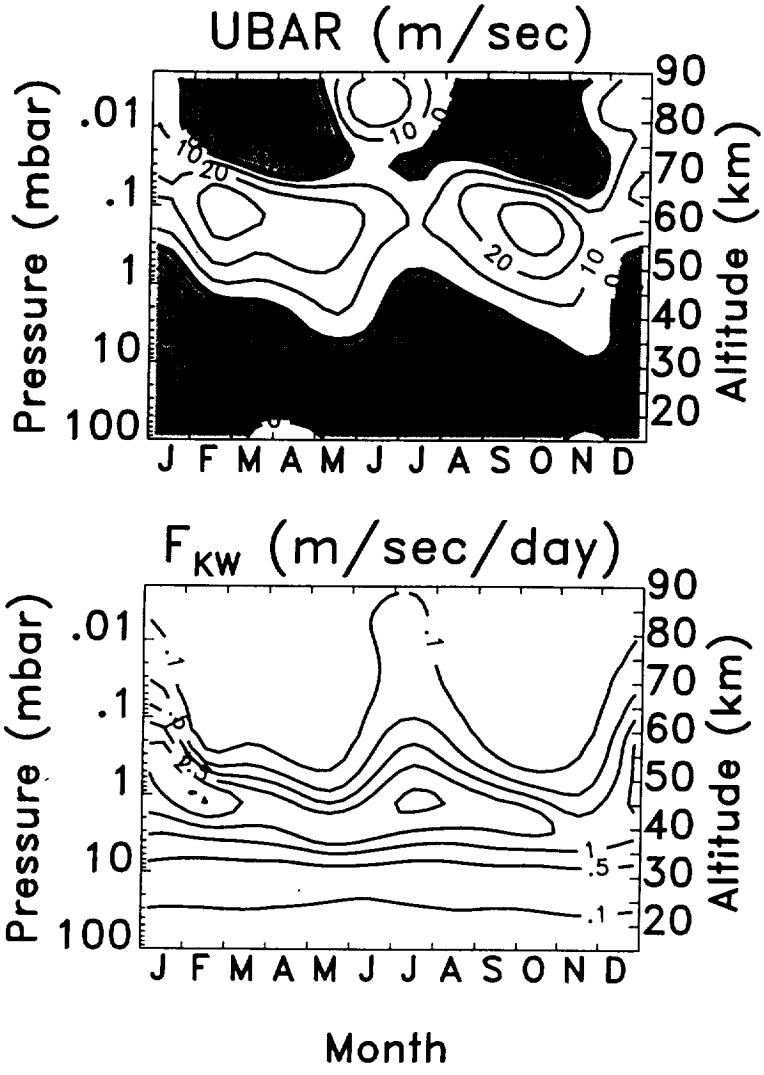

FIGURE A.8

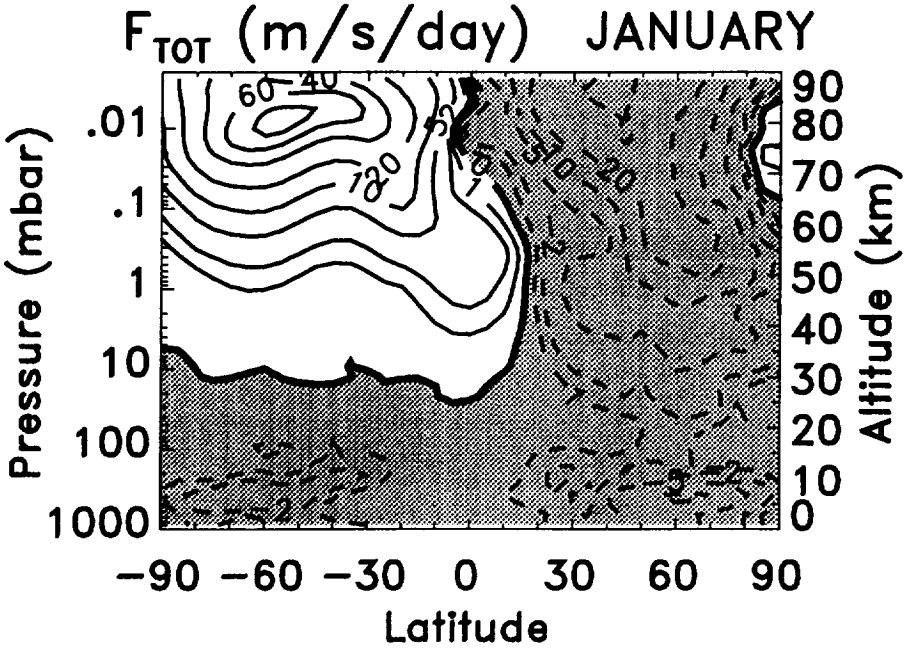
F_{TOT} (m/s/day) JANUARY
Pressure (mbar)
.01
.1
1
10
100
1000
Altitude (km)
90
80
70
60
50
40
30
20
10
0
−90 −60 −30 0 30 60 90
Latitude
60
40
20
0
−20
−40
−60
−80
−100
−120
−140
−160
−180

FIGURE A.9